nature communications

Article

https://doi.org/10.1038/s41467-025-56414-8

Assembly of Genetically Engineered Ionizable Protein Nanocage-based Nanozymes for Intracellular Superoxide Scavenging

Received: 19 January 2024

Accepted: 17 January 2025

Published online: 28 January 2025

Check for updates

Qiqi Liu[1,2,4], Zhanxia Gao[1,4], Xiangyun Zhang[2,4], Qiannan Duan[2], Yue Zhang[3], Adam C. Midgley[2], Li Jiao[2], Ruming Liu[2], Mingsheng Zhu[2], Deling Kong[2] ✉, Jie Zhuang[1] ✉ & Xinglu Huang[2] ✉

Nanozymes play a pivotal role in mitigating excessive oxidative stress, however, determining their specific enzyme-mimicking activities for intracellular free radical scavenging is challenging due to endo-lysosomal entrapment. In this study, we employ a genetic engineering strategy to generate ionizable ferritin nanocages (iFTn), enabling their escape from endo-lysosomes and entry into the cytoplasm. Specifically, ionizable repeated Histidine-Histidine-Glutamic acid ($9H_2E$) sequences are genetically incorporated into the outer surface of human heavy chain FTn, followed by the assembly of various chain-like nanostructures via a two-armed polyethylene glycol (PEG). Utilizing endosome-escaping ability, we design iFTn-based tetrameric cascade nanozymes with high superoxide dismutase- and catalase-mimicking activities. The in vivo protective effects of these ionizable cascade nanozymes against cardiac oxidative injury are demonstrated in female mouse models of cardiac ischemia-reperfusion (IR). RNA-sequencing analysis highlight the crucial role of these nanozymes in modulating superoxide anions-, hydrogen peroxide- and mitochondrial functions-relevant genes in IR injured cardiac tissue. These genetically engineered ionizable protein nanocarriers provide opportunities for developing ionizable drug delivery systems.

Ischemia-reperfusion (IR) injury, which typically occurs following restoration of blood flow to previously ischemic tissues, contributes to mortality and morbidity in a wide variety of clinical pathologies, including myocardial infarction, trauma, ischemic stroke, and post-cardiac arrest syndrome[1,2]. Although the detailed pathogenic mechanisms of IR injuries are not completely understood, excessive production of reactive oxygen species (ROS) has been implicated as a considered determinative factor in the induction of IR tissue injury[3–5]. In other words, the burst of superoxide anions ($O_2^{\cdot-}$) from the mitochondrial respiratory chain during reperfusion has been well-characterized as the main initiating factor. Consequently, development of approaches to scavenge $O_2^{\cdot-}$ is essential to alleviate IR injury.

[1]School of Medicine, Nankai University, Tianjin 300071, China. [2]Key Laboratory of Bioactive Materials for the Ministry of Education, College of Life Sciences, State Key Laboratory of Medicinal Chemical Biology, and Frontier of Science Center for Cell Response, Nankai University, Tianjin 300071, China. [3]Tianjin Key Laboratory of Cellular Homeostasis and Disease, Department of Physiology and Pathophysiology, Tianjin Medical University, Tianjin 300070, China. [4]These authors contributed equally: Qiqi Liu, Zhanxia Gao, Xiangyun Zhang. ✉e-mail: kongdeling@nankai.edu.cn; zhuangj@nankai.edu.cn; huangxinglu@nankai.edu.cn

Superoxide dismutase (SOD) and catalase (CAT) serve as the primary antioxidant enzymes against $O_2^{\cdot-}$-induced oxidative stress. Typically, SOD catalyzes the conversion of $O_2^{\cdot-}$ to O_2 and H_2O_2, while CAT decomposes H_2O_2 to O_2 and H_2O. However, the biomedical application of natural antioxidant enzymes has been limited by the high cost of protein preparation, their susceptibility to inactivation, and their low membrane permeability[6–8].

Nanozymes represent an emerging class of artificial enzymes, offering advantages such as low cost, high stability, multifunctionality and membrane permeability[9–12]. By mimicking the activities of natural enzymes, nanozymes have demonstrated potential in treating various diseases by either generating or scavenging cytotoxic free radicals, such as in cancer therapy[13–15], bactericidal actions[16,17], and abatement of myocardial IR injury[18]. However, leveraging nanozymes to mitigate IR injury encounters challenges, primarily due to limitations in their environment-dependent enzyme-mimicking activities. Specifically, the same nanozyme that possesses free radical-scavenging ability under physiological conditions may also exhibit free radical-production under acidic conditions[11,13,19,20]. Upon delivery to damaged cells in IR tissue, nanozymes are readily entrapped in endo-lysosomes after uptake, and the endo-lysosomal acidic environment induces an over-production of free radicals. Thus, the development of strategies for escape from endo-lysosomes and subsequent entry into the cytoplasm is essential for the effective application of nanozymes in the alleviation of IR injury.

In this work, we develop endosome-escaping nanozymes by harnessing genetically engineered ionizable human heavy chain ferritin nanocage (iFTn), achieved through the genetic incorporation of ionizable repeated Histidine-Histidine-Glutamic acid ($9H_2E$) sequences. Using a two-armed polyethylene glycol (PEG) crosslinker, we assemble iFTn into various chain-like nanostructures and compare their ionizable performance and endosome-escaping effect in H9C2 cells. We use mouse cardiac IR injury as a model to assess the in vivo advantages of iFTn tetrameric assemblies for targeted delivery to ischemic cardiac tissue. The protective effects against IR injury are evaluated through their corresponding nanozymes with SOD-mimicking activity. To improve free radical conversion, we assemble a tetrameric cascade nanozyme consisting of two SOD- and two CAT-like nanozymes, enabling the cascade conversion of $O_2^{\cdot-}$ into non-toxic O_2 and H_2O. We investigate the enhanced protective ability of these cascade nanozymes in a mouse cardiac IR injury model, comparing them to nanozymes with only SOD- or CAT-like activity. Finally, we explore the potential protective mechanisms of the cascade nanozymes against cardiac IR injury through RNA sequencing and analysis.

Results

Assembly of ionizable protein nanocages

Human recombinant ferritin heavy chains can spontaneously assemble into protein nanocages, each composed of 24 heavy chain subunits. This is achievable in *E. Coli*, using a recombinant protein expression strategy[21–24]. In the present study, we utilized a genetically engineered approach to incorporate an ionizable peptide into the N-terminus of the ferritin heavy chain, which results in the display of the ionizable peptide on the outer surface of FTn, resulting in the formation of iFTn after assembly with FTn subunits (Fig. 1a). Specifically, the ionizable peptide consisted of nine repeated Histidine-Histidine-Glutamic acid sequences (i.e., $9H_2E$), capable of ionization under acidic pH conditions due to histidine's approximate pKa of 6.0, thereby endowing a mechanism facilitating the endosomal escape of iFTn[25]. Protein structure prediction using AlphaFold2 indicated that the fusion of $9H_2E$ to the N-terminus of FTn resulted in a linear disordered structure displayed on the surface of iFTn (Fig. 1b), which suggested there would be no interference with folding of FTn subunits. However, the incorporation of $9H_2E$ led to a decrease in the cellular uptake of FTn in H9C2 cardiomyocytes. Among five iFTn constructs (Supplementary Fig. 1a), iFTn containing 30% H_2E-FTn subunits was screened as the optimal protein nanocages to achieve a balance between an ionizable property (Supplementary Fig. 1b) and satisfactory cellular uptake (Supplementary Fig. 1c). The optimal iFTn was utilized for all subsequent studies, unless otherwise indicated. We then sought to synthesize iFTn into various iFTn-*N*er assemblies by using two-armed PEG crosslinkers - a methodology we had previously established[26]. Briefly, after reacting two-armed PEG-succinimidyl carboxylmethyl ester (SCM) with free primary amine ($-NH_2$) groups of iFTn, various assemblies were obtained through gel purification. Transmission electron microscopy (TEM) images showed different lengths of various chain-like assemblies (Fig. 1c), including iFTn-1er (11.0 nm), iFTn-2er (20.1 nm), iFTn-3er (29.7 nm) and iFTn-4er (40.6 nm). Different molecular sizes of the four assemblies were further confirmed by native-PAGE gel analysis (Fig. 1d). Size exclusion chromatography analysis also illustrated the larger molecular sizes of various assemblies compared to iFTn and FTn (Fig. 1e). Importantly, the various assemblies exhibited a gradual improvement in ionizable ability with the increase of incorporated iFTn, as evidenced by 6.2 mV for iFTn-1er, 7.1 mV for iFTn-2er, 8.8 mV for iFTn-3er and 9.5 mV for iFTn-4er at pH 5.0, respectively (Fig. 1f). In contrast, positive charges of various iFTn assemblies were not observed at pH 7.2, remaining stable within the range of -10 ~ -20 mV.

Subsequently, we sought to compare the intracellular behaviors of different iFTn assemblies. To do this, iFTn was pre-labeled with Cy5 and then assembled with non-labeled iFTn to form various iFTn assemblies through a two-armed PEG, resulting in an equal molar amount of Cy5-labeled iFTn in different assemblies. After incubation with H9C2 cells (Fig. 2a) and isolated primary mouse neonatal cardiomyocytes (Supplementary Fig. 2), confocal images showed the distribution of various iFTn assemblies within the cells. Flow cytometry analysis illustrated an increase in signal intensity in cells corresponding to the elevated number of iFTn assemblies (Fig. 2b). Compared to iFTn and iFTn-2er, the uptake of iFTn-4er exhibited an approximately 2.0- and 1.2-fold improvement, respectively. Following uptake, we further explored whether various iFTn assemblies were able to escape from endo-lysosomes (Fig. 2c). The various Cy5-labled iFTn assemblies were incubated with cardiomyocytes for 2 hours, and following the removal of excess, cells were cultured for an additional 2 hours before fixation and confocal microscopy visualization of Cy5 and LysoTracker stained lysosomes. The images showed the co-localization of the different iFTn assemblies and lysosomes (Fig. 2d). Compared to native FTn alone, enhanced endo-lysosomal escape capabilities of the various iFTn assemblies were observed. Further quantification analysis of the colocalization using the Pearson's coefficient demonstrated that the iFTn-4er localized in lysosomes decreased by 22% and 18% compared to iFTn-1er and iFTn-2er, respectively. Furthermore, we monitored the colocalization and lysosomal escaping efficacy of iFTn-4er and its non-ionizing counterpart, FTn-4er, with LysoTracker at 0, 1, 2, 3, and 4 hours post-internalization (Fig. 2e). During the initial 0 - 1 hour period, both iFTn-4er and FTn-4er displayed similar levels of colocalization with lysosomes. However, beyond 1 hour, iFTn-4er exhibited a significantly greater reduction in colocalization compared to FTn-4er (Fig. 2f). Quantification analysis of fluorescence signals in cytoplasm (excluding lysosomes) relative to total intracellular signals indicated that approximately 60% of iFTn-4er successfully escaped from lysosomes, whereas FTn-4er remained largely confined, with only 20% escaping (Fig. 2g). These results revealed the ionizable properties of various iFTn assemblies facilitated their escape from endo-lysosomes, and this phenomenon was dependent on positively charges of iFTn particles within the endo-lysosomal microenvironment (i.e., pH 5.0-5.5).

Preparation and in vitro protective effect of iFTn nanozymes

The excessive production of superoxide radicals ($O_2^{\cdot-}$) plays essential roles in driving intracellular oxidative stress. Nanozymes with

https://doi.org/10.1038/s41467-025-56414-8

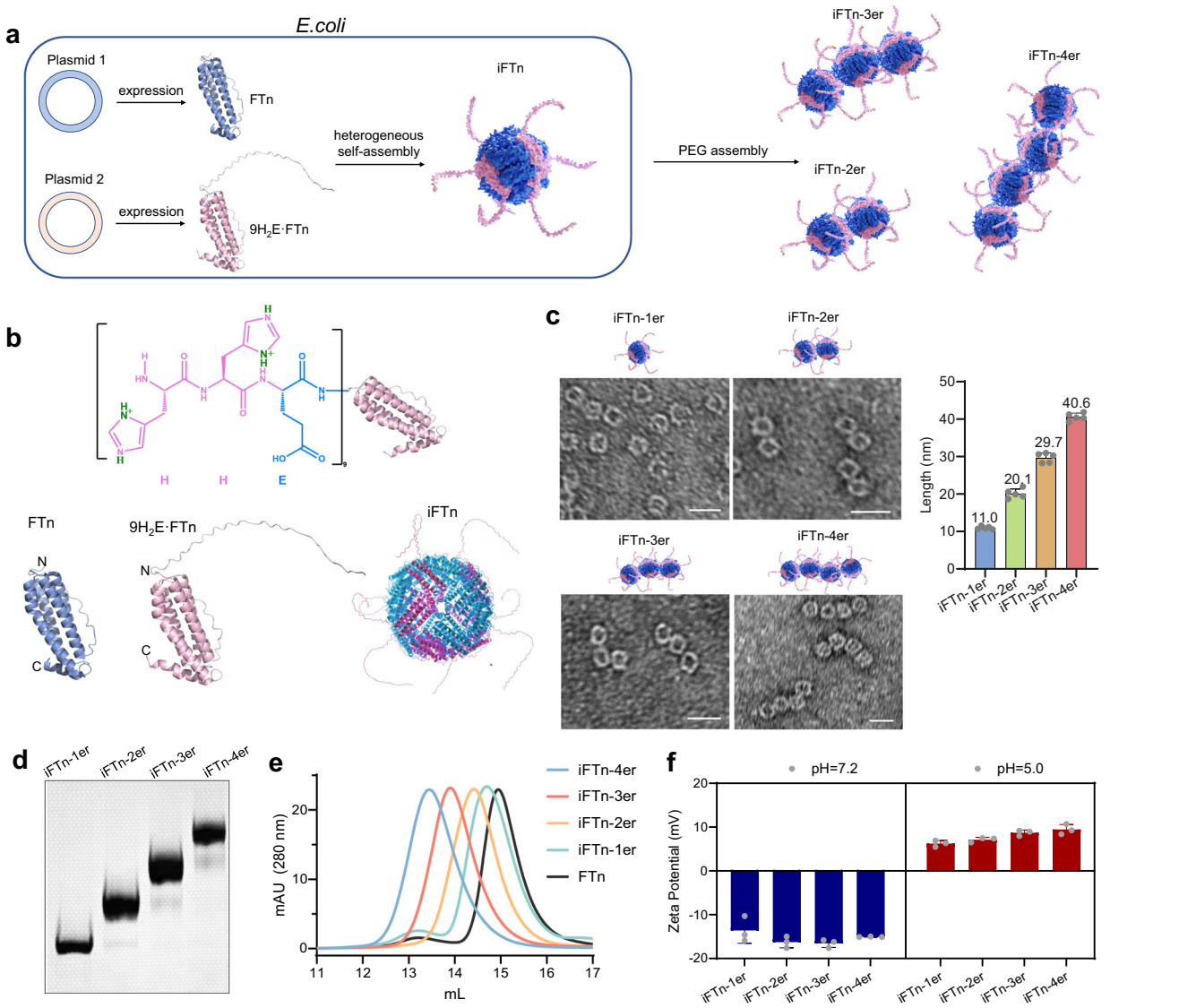

Fig. 1 | Assembly and characterization of iFTn. a Schematic illustration depicting the assembly process of iFTn through a two-step self-assembly/post-assembly approach. Firstly, iFTn, assembled by expressed FTn and $9H_2E$·FTn subunits at a specific ratio in *E. coli*, were obtained through self-assembly. Subsequently, these iFTn were further assembled into various iFTn assemblies using a two-armed PEG crosslinker. **b** Protein structure of iFTn: upper illustrates $9H_2E$ peptides incorporated into N-terminus of FTn. Lower displays the protein structures of FTn and $9H_2E$·FTn subunit generated by Alphafold 2. **c** TEM images showing chain-like structures of iFTn and its assemblies. Scale bar = 20 nm. The right panel presents a quantification analysis of the length of various assembled iFTn ($n = 5$ technical samples examined over three biologically independent experiments). **d** Native-PAGE gel electrophoretic analysis of iFTn and its assemblies. **e** Size exclusion chromatography analysis of iFTn and its assemblies in protein purification equipment. **f** Zeta potential of iFTn and its assemblies at pH 7.2 and pH 5.0 ($n = 3$ independent experiments). Data are presented as mean values ± SD. Source data are provided as a Source Data file.

SOD-mimicking activities are effective in scavenging cytotoxic $O_2^{\cdot-}$. Recently, we employed FTn as a protein scaffold for designing $O_2^{\cdot-}$-scavenging nanozymes due to its ability to actively bind with metal ions[7]. Thus, MnO_2 nanozymes were in situ incorporated into the cavity of iFTn (i.e., iFTn-M), using a biomineralization approach, and then were further assembled to form various chain-like iFTn-M assemblies using two-armed PEG crosslinkers, yielding iFTn-M1, iFTn-M2, iFTn-M3 and iFTn-M4 (Fig. 3a). Unstained native-PAGE analysis revealed the visualization of brown nanozyme particles, and the protein shell was shown at the same location after staining with Coomassie Blue (Fig. 3b). Importantly, the electrophoretic migration rates of various iFTn-M assemblies were consistent with their corresponding iFTn assemblies. TEM imaging confirmed the structure of chain-like nanozyme assemblies with a 6 nm diameter MnO_2 core (Fig. 3c). We next determined whether iFTn-M assemblies possessed SOD-mimicking activity, catalyzing the conversion of $O_2^{\cdot-}$ into O_2. The SOD-like activities of various iFTn-M assemblies, each at identical molar concentrations, were evaluated using the xanthine/xanthine oxidase system to generate $O_2^{\cdot-}$. As illustrated in Fig. 3d, all iFTn-M assemblies demonstrated the ability to scavenge $O_2^{\cdot-}$, with iFTn-M4 showing the highest activity, indicating its superior SOD-like activity. This was further validated by direct measurement of $O_2^{\cdot-}$ using electron paramagnetic resonance (EPR), which confirmed that iFTn-M4 effectively scavenged the $O_2^{\cdot-}$ generated by the xanthine/xanthine oxidase system (Fig. 3e).

Next, we investigated the protective effect of iFTn-M nanozymes against intracellular oxidative stress in cardiomyocytes. To do this, H9C2 cells were firstly exposed to hypoxia-reoxygenation (H/R) treatment to induce oxidative stress. Following various treatments, the total level of ROS in H9C2 cells was analyzed using a ROS probe,

https://doi.org/10.1038/s41467-025-56414-8

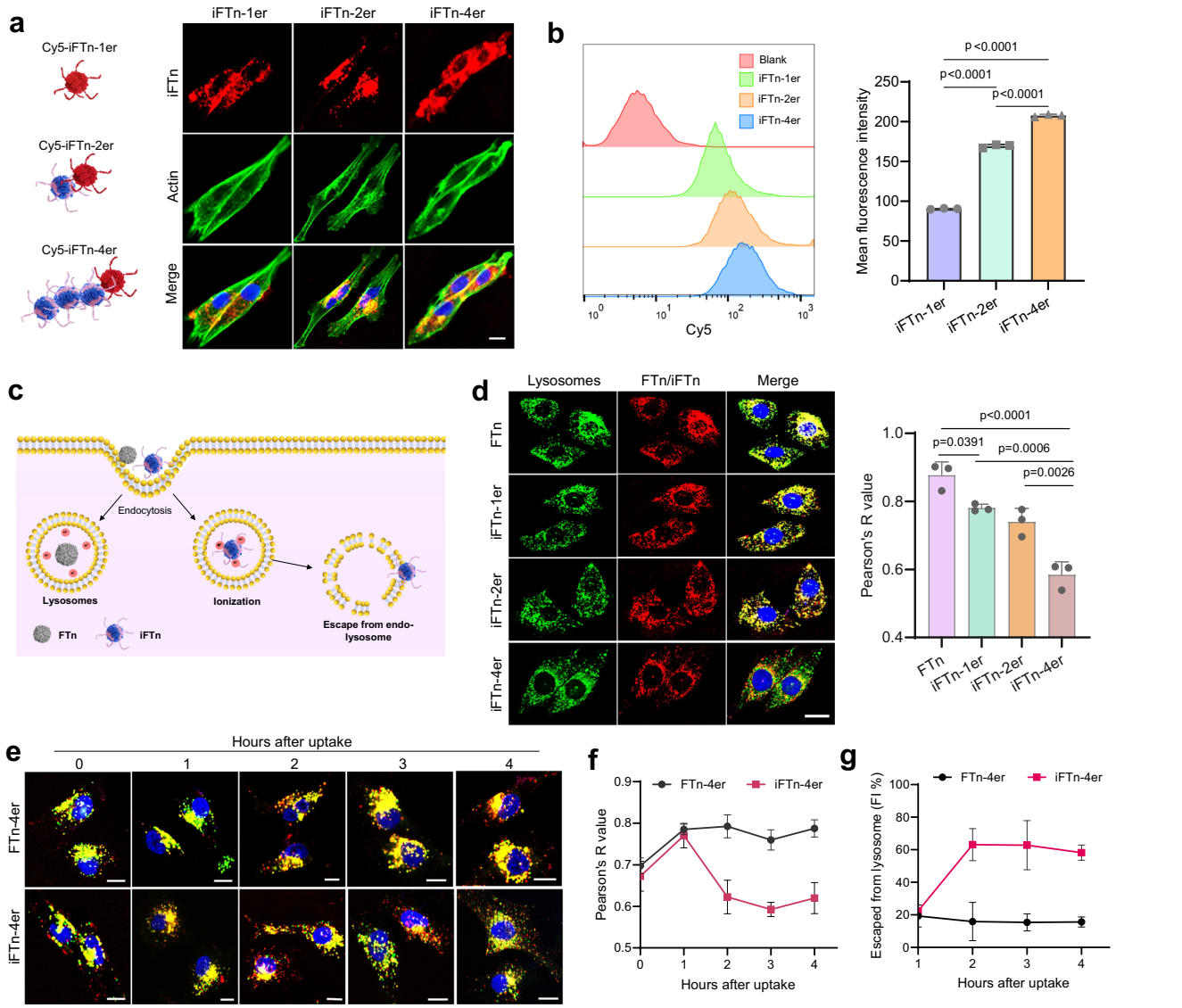

Fig. 2 | Intracellular behaviors of iFTn assemblies. a Confocal imaging illustrating the cellular uptake of iFTn and its assemblies in H9C2 cells. The assemblies were obtained using the identified Cy5-labeled iFTn (left). Cell morphology was visualized with phalloidin staining (green). Scale bar = 10 μm. **b** Quantification analysis of cellular uptake of various iFTn assemblies by flow cytometry ($n = 3$ independent biological experiments). **c** Schematic illustration of iFTn escaping from endo-lysosome due to their ionizable property, while FTn is easily trapped into lysosome after uptake. **d** Confocal images depicting the colocalization of FTn and various iFTn (red) with lysosomes (green). Scale bar = 10 μm. Right shows quantification analysis of particle colocalization with lysosomes was performed using Pearson's coefficient ($n = 3$ biologically independent experiments). **e** Confocal images depicting the colocalization of FTn-4er/iFTn-4er (red) with lysosomes (green). Scale bar = 10 μm. **f** Quantification analysis of iFTn-4er and FTn-4er colocalization with lysosomes was performed using Pearson's coefficient ($n = 4$ biologically independent experiments). **g** Quantification analysis of the percentage of iFTn-4er and FTn-4er escaped from lysosomes ($n = 3$ biologically independent experiments). The data calculated by the mean fluorescence intensity of nanoparticles in the cytoplasm (excluding lysosomes) to the total fluorescence intensity in the cells. Data are presented as mean values ± SD. p values are calculated using one-way ANOVA with Tukey's multiple comparisons test without adjustments (**b**, **d**). Source data are provided as a Source Data file.

dichloro-dihydro-fluorescein diacetate (DCFH-DA)[27]. Confocal images and relative quantification analysis by flow cytometry revealed a marked reduction in fluorescence signal intensity after treatment with iFTn-M nanozymes, especially in the iFTn-M4 treatment group, indicating that iFTn-M4 exhibited a significantly greater ROS scavenging ability compared to iFTn-M1 and iFTn-M2 (Supplementary Fig. 3). These findings were further validated using isolated primary cardiomyocytes (Supplementary Fig. 4). Dihydroethidium (DHE), an $O_2^{\cdot-}$ probe, can intercalate within DNA for nucleus staining following its oxidization in cells. Confocal images revealed strong red fluorescence (oxidized DHE) in H9C2 cells subjected to H/R-induced oxidative stress, whereas untreated cells showed only faint fluorescence (Fig. 3f). Under the same H/R conditions, the addition of FTn/iFTn MnO_2 nanozymes effectively scavenged $O_2^{\cdot-}$, with iFTn-M4 exhibiting the superior scavenging ability. Flow cytometry analysis illustrated that there were approximately 58% reductions in $O_2^{\cdot-}$ following treatment with iFTn-M4, respectively (Fig. 3g). Importantly, iFTn-M4 were significantly more effective than their non-ionizable counterparts (i.e., FTn-M4) ($p = 0.0355$). Furthermore, we explored whether these nanozymes protected the cells from oxidative damage. The mitochondrial function was first evaluated by analyzing mitochondrial DNA (mtDNA) copy number via qPCR. There was an elevated protective effect on mtDNA in the iFTn-M4 treatment group, compared to that of FTn-M assemblies, iFTn-M1 and iFTn-M2 (Fig. 3h). Cell apoptosis induced by H/R oxidative stress was also analyzed with or without nanozyme treatments. We observed that oxidative damage induced

https://doi.org/10.1038/s41467-025-56414-8

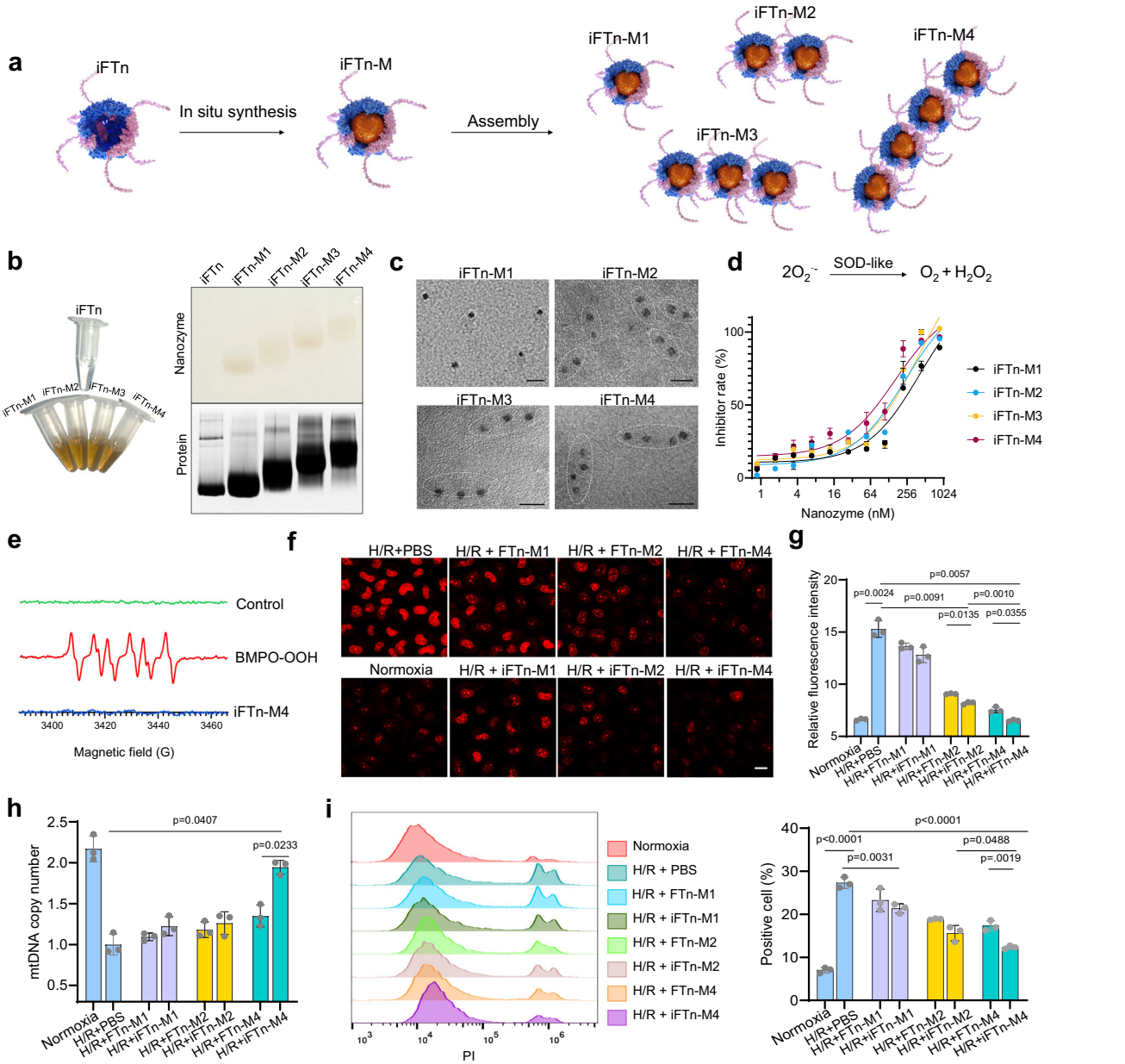

Fig. 3 | Preparation and in vitro protective effect of iFTn-M nanozymes against oxidative stress. a Schematic illustration depicting the preparation process of iFTn-M nanozymes. **b** Visualization of iFTn-M nanozymes. Left, iFTn-M showing a brown color after incorporation of nanozymes. Right, Native-PAGE analysis of different iFTn-M nanozymes. Brown MnO_2 nanozymes are visibly present in the unstained gel (upper). After protein staining with Coomassie Blue, colocalization of protein is observed (lower). **c** TEM images showing the chain-like nanostructures (dash line) of iFTn-M nanozymes. Scale bar = 10 nm. **d** Kinetics of $O_2^{\cdot-}$ scavenging by various iFTn-M nanozymes were assessed under the same conditions using the xanthine/xanthine system ($n = 3$ biologically independent experiments). **e** EPR spin trapping using BMPO in the xanthine/xanthine oxidase system and following incubation with iFTn-M4. **f** Representative confocal images showing intracellular $O_2^{\cdot-}$ levels in H9C2 cells using DHE staining, which intercalates with DNA for nucleus staining showing a bright red fluorescent (oxidized DHE). Scale bar = 10 μm. **g** Quantification analysis of cellular $O_2^{\cdot-}$ levels by flow cytometry after different treatments ($n = 3$ biologically independent experiments). **h** qPCR analysis of mtDNA copy number in H9C2 cells following different treatments ($n = 3$ biologically independent experiments). **i** Flow cytometry (left) and quantification analysis (right) of H9C2 cells stained with Propidium Iodide (PI) to assess apoptosis levels after various treatments ($n = 3$ biologically independent experiments). p values are calculated using two-way ANOVA with Tukey's multiple comparisons test without adjustments (**g**–**i**). Data are presented as mean values ± SD. Source data are provided as a Source Data file.

approximately 28% cell apoptosis, which was reduced upon the addition of various FTn MnO_2 nanozymes (Fig. 3i). Notably, treatment with iFTn-M4 resulted in a 57% reduction in cell apoptosis induced by oxidative stress, a significantly greater effect compared to iFTn-M1, iFTn-M2 and non-ionizable FTn-M nanozymes. These collective data reveal the advantage of ionizable FTn-based tetrameric nanozymes over other nanozymes (e.g., non-ionizable counterparts, monomers and dimers) in protecting cells from oxidative stress damage.

Accumulation and cardiac repair of iFTn nanozymes in mouse IR model

Considering the burst release of $O_2^{\cdot-}$ as an initiating factor for cardiac tissue IR injury, we next sought to study whether iFTn-M nanozymes could enhance cardiac tissue repair in a mouse IR myocardial injury model. First, we explored the in vivo biodistribution of various Cy5-labeled iFTn using an IVIS imaging system after intravenous (*i.v.*) administration during IR injury. At 12 hours and 24 hours, ex vivo

https://doi.org/10.1038/s41467-025-56414-8

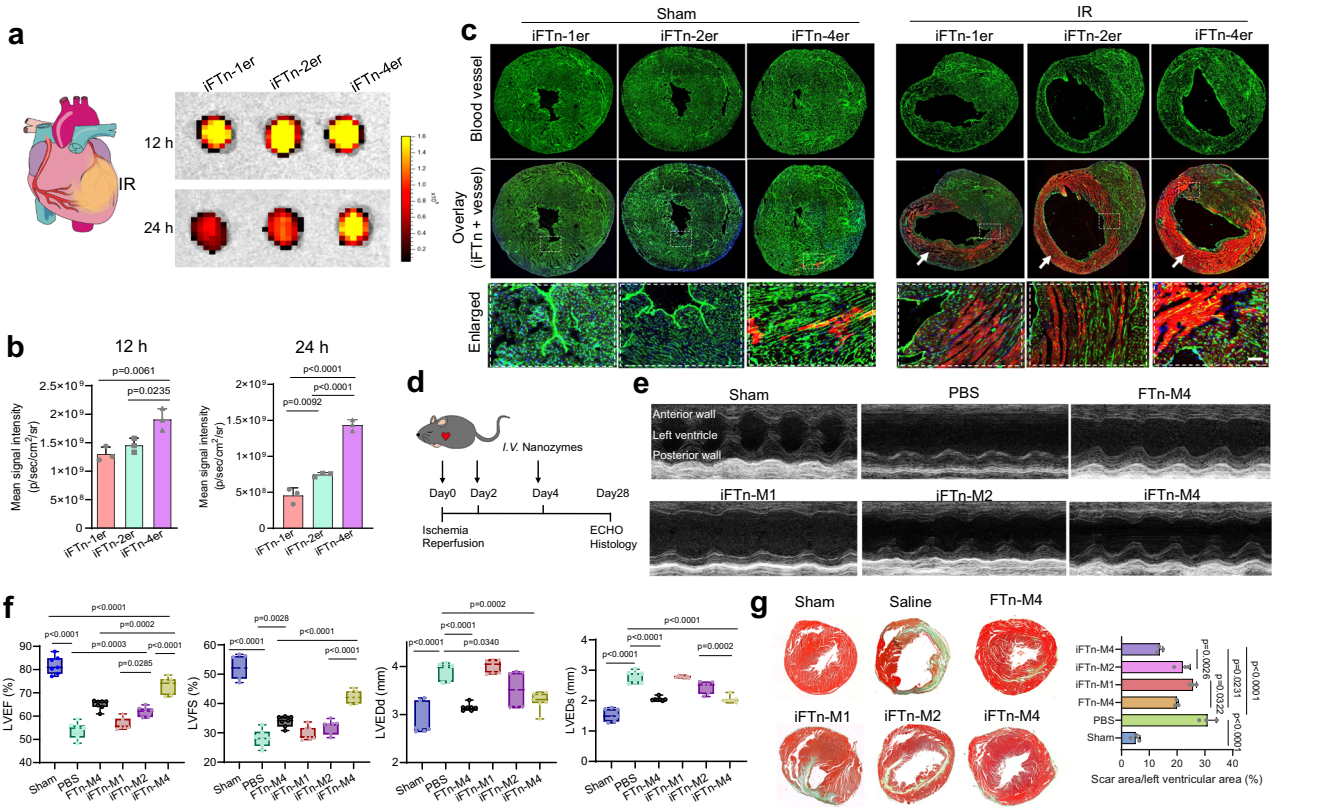

Fig. 4 | Accumulation and cardiac repair of iFTn-M nanozymes in a mouse IR model. a Ex vivo fluorescent images of Cy5-labeled iFTn assemblies in harvested IR hearts of mice 12 h (upper) and 24 h (lower) after tail vein injection. These hearts were collected from the same mice for assessing biodistribution, as shown in Supplementary Fig. 5. **b** Quantitative analysis of fluorescence intensities of IR hearts from (a) ($n = 3$ mice for each group). **c** Fluorescence imaging of various Cy5-labeled iFTn distribution (red) in sham and IR cardiac tissue 24 hours after tail vein injection. The reconstructed cardiac panorama and enlarged area are shown in the upper and lower panels, respectively. Blood vessels are marked with an anti-CD31 antibody (green) ($n = 3$ mice for each group). Scale bar = 100 μm. **d** Schematic diagram of the assessment and the therapeutic intervention procedures. **e** ECHO images of left ventricular wall motion in mice with different treatments following IR surgery at 28 days ($n = 7$ mice per group). **f** Quantification analysis of cardiac function by determining the parameters of left ventricular ejection fractions (LVEFs), left ventricular fractional shortening (LVFS), left ventricular end-diastolic diameter (LVEDd) and left ventricular end-systolic dimension (LVEDs) ($n = 7$ mice per group). **g** Representative images (left) of midpapillary regions of the hearts, 28 days after IR using Masson's staining (green represents collagen-rich scar tissue, red represents viable myocardium). Right showing quantification analysis of the injury level by calculating the percentage of the scar area relative to the left ventricular area ($n = 3$ in each group). Data are presented as mean values ± SD. p values are calculated using one-way ANOVA with Tukey's multiple comparisons test without adjustments (**b**, **f**, **g**). Source data are provided as a Source Data file.

imaging illustrated that various iFTn assemblies were primarily distributed in liver, with no significant differences among the different assemblies (Supplementary Fig. 5). Importantly, a significant accumulation of various iFTn assemblies were observed in the isolated IR hearts following *i.v.* administration (Fig. 4a). Quantitative analysis demonstrated that iFTn-4er had slightly higher accumulation than iFTn-2er and iFTn-1er (Fig. 4b). Assessment at 24 hours indicated that the accumulation difference between iFTn-4er and other iFTn assemblies was larger, with a 2-fold stronger signal intensity in the iFTn-4er group compared to iFTn-2er group ($p < 0.0001$). These results suggest that iFTn-4er exhibited enhanced accumulation and retention ability in the IR heart, and this was expected, primarily due to the longer blood circulation time of iFTn-4er that we previously reported[26]. To further understand their accumulation in the IR heart, we compared the tissue distribution of various iFTn assemblies in sham and IR hearts. After injecting Cy5-labeled iFTn, the hearts were harvested 24 hours later for cryosection, followed by blood vessel immunostaining and manual reconstruction of the cardiac tissue panorama. As previously reported[25], IR induced microvascular damage, leading to reduced vascular density in the heart and noticeable left ventricular enlargement (Fig. 4c), indicating the successful generation of IR injured heart models. In the sham hearts, the signal from various Cy5-iFTn was negligible. In contrast, the signal from various Cy5-iFTn in the injured area was significantly enhanced compared to the sham heart tissue. In particular, in the same IR cardiac tissue, various Cy5-iFTn primarily accumulated in the injured area (white arrow) but not in the non-injury area. Consistent with the results of ex vivo imaging, iFTn-4er exhibited the highest particle distribution in IR cardiac tissue. These findings suggest that the improved accumulation ability of iFTn in IR-damage tissue may be attributed to enhanced vascular permeability in injured vessels and elevated expression of FTn receptor in ischemic damaged tissue[18,28].

Next, we assessed the therapeutic efficacy of iFTn-M assemblies by administering three doses of one of the following treatments via *i.v.* injection: PBS, FTn-M4, iFTn-M1, iFTn-M2 or iFTn-M4. At 28 days post-IR surgery, we conducted echocardiography (ECHO) and histological evaluations to assess heart functions (Fig. 4d). The M-model ECHO images depicted the motion of the left ventricular wall in sham mice and IR mice subjected to different treatments, indicating varying levels of contraction functional damage in the anterior/posterior walls (Fig. 4e). Corresponding quantitative analysis revealed that the parameters of left ventricular ejection fraction (LVEF) and left ventricular fractional shortening (LVFS) in the PBS treatment group had reduced to approximately 50% of the sham mice, as expected (Fig. 4f).

Compared to PBS treatment, a gradual improvement in the recovery of heart functionality was observed when mice were administered FTn-M4, iFTn-M1, iFTn-M2, and iFTn-M4, as evidenced by the improved parameters of LVEF, LVFS, left ventricular end-diastolic diameter (LVEDd) and left ventricular end-systolic dimension (LVEDs). Subsequently, hearts were isolated for further evaluation of tissue fibrosis using Masson's trichrome staining. We observed a significant reduction in collagen deposition in mice treated with iFTn-M4 compared to those in the PBS, FTn-M4, iFTn-M1, and iFTn-M2 groups (Fig. 4g). Quantification analysis revealed that while more than 31% of the scar area relative to left ventricular area was damaged in mice treated with PBS, this decreased to 19%, 25%, 22% and 14% following treatments with FTn-M4, iFTn-M1, iFTn-M2 and iFTn-M4, respectively. Based on these findings, the optimized tetrameric iFTn assemblies were utilized for the subsequent construction of cascade nanozymes.

Construction of iFTn cascade nanozymes

Enzyme cascade reactions facilitate the improvement of free radical conversion efficacy. SOD catalyzes the conversion of $O_2^{\cdot-}$ to O_2 and H_2O_2, and H_2O_2 is further converted into non-toxic O_2 and H_2O by CAT. Thus, an ideal nanozyme should be highly efficient in catalyzing the conversion of $O_2^{\cdot-}$ into non-toxic O_2 and H_2O by possessing both SOD- and CAT-like activities. Inspired by this concept and the benefits of iFTn tetrameric nanozymes (i.e., iFTn-M4), we further constructed an iFTn tetrameric cascade nanozyme by incorporating the high SOD-like activity of iFTn-M and the high CAT-like activity of iFTn-Ru nanozyme (iFTn-R) (Fig. 5a). Specifically, the cascade nanozyme was randomly assembled by the same molar ratio of iFTn-M and iFTn-R through a two-armed PEG. Theoretically, a typical assembly contained four iFTn nanozymes consisting of two iFTn-M and two iFTn-R (iFTn-MR4), allowing for cascade conversion of $O_2^{\cdot-}$ into non-toxic O_2 and H_2O. TEM images showed the formation of metal nanoparticles within the iFTn, resulting in iFTn-M and iFTn-R with diameters of approximately 6 nm and 1.5 nm, respectively (Fig. 5b). The variation in size between iFTn-M and iFTn-R can be attributed to differences in synthetic approaches, as described in our previously report[7]. Furthermore, the assembled iFTn-MR4 via PEG crosslinkers exhibited chain-like nanostructures comprising iFTn-M and iFTn-R of different sizes. To facilitate evaluate the therapeutic potentials of iFTn-MR4, tetrameric iFTn-M4 and tetrameric iFTn-R4 were also constructed as control nanozymes. The SOD- and CAT-like activities of iFTn-M4, iFTn-R4, and iFTn-MR4 were evaluated using Michaelis-Menten kinetics, a model of enzymatic dynamics. As expected, the SOD-like activity of iFTn-R4 was negligible (Fig. 5c), while its CAT-like activity was significantly higher than iFTn-M4 under the same reaction conditions (Fig. 5d). Importantly, the iFTn-MR4 combined the advantages of the two types of nanozymes, exhibiting both high SOD- and CAT-like activities. The detailed IC_{50} (half-maximal inhibitory concentration) and k_{cat} (turnover number, the catalytic constant for the conversion of substrate to product), two important parameters of enzyme catalytic efficiency, are listed in Fig. 5e.

It is well known that IR injury can induce mitochondrial dysfunction due to ROS overproduction[29]. We next assessed the protective potential of nanozymes against IR damage, including intracellular oxygen levels, mitochondrial permeability transition pore (mPTP) and mitochondrial DNA (mtDNA) copy number (Fig. 5f). The $[Ru(dpp)_3]Cl_2$ is a viable oxygen probe, and its luminescence is strongly quenched by molecular oxygen[30]. Using this probe, we evaluated the intracellular O_2 levels under H/R-induced oxidative stress in H9C2 cardiomyocytes. Confocal images illustrated a significant elevation of oxygen levels after treatment with iFTn-MR4 compared to PBS, iFTn-M4, and iFTn-R4, as evidenced by reduced signal intensity of the probe (Fig. 5g). Further quantitative analysis by flow cytometry confirmed that iFTn-MR4 significantly improved intracellular oxygen levels ($p < 0.001$), whereas iFTn-M4 and iFTn-R4 exhibited limited effects (Fig. 5h). Calcium overload leads to the opening of mPTP in the mitochondrial inner membrane, especially when accompanied by oxidative stress[31]. Confocal images revealed that iFTn-MR4 facilitated alleviation of the opening of mPTP under H/R-induced oxidative stress, as evidenced by the detection with Calcein AM (Fig. 5i). Furthermore, qPCR analysis of mitochondrial DNA (mtDNA) copy number was conducted to assess mitochondrial function. The elevated protective effect of iFTn-MR4 on mitochondrial function was significantly better than iFTn-M4 and iFTn-R4 (Fig. 5j). These results suggest that the iFTn-MR4 efficiently eliminates intracellular ROS by both SOD- and CAT-like activities, thereby protecting mitochondrial functions in cardiomyocytes subjected to oxidative stress.

In vivo cardiac protection of iFTn cascade nanozymes in IR mouse model

We next investigated whether iFTn-MR4 cascade nanozymes would provide a synergistic protective effect against cardiac IR injury. First, we assessed their acute protective effects using M-mode echocardiography at 1 and 3 days post-surgery (Supplementary Fig. 6). Assessment of left ventricle functional parameters, including LVEF, LVFS, LVEDd and LVEDs, revealed a gradual improvement in cardiac function with iFTn-R4, iFTn-M4, and iFTn-MR4 treatment during these early stages post-IR injury. Additionally, to assess cardiac tissue damage, we performed triphenyl tetrazolium chloride (TTC) staining on six tissue samples from each heart 24 hours after *i.v.* nanozyme administration (Fig. 6a). Infarct size, indicated by white-stained areas, was prominently observed in the hearts subjected to IR, particularly in the PBS-treated group (Fig. 6b). Quantitative analysis of the infarct size in each slice demonstrated a significant reduction in the infarcted area of IR tissue treated with different iFTn nanozymes compared to PBS-treated IR tissue. Importantly, iFTn-MR4 exhibited a synergistic protective effect against cardiac IR injury compared to iFTn-M4 or iFTn-R4 alone.

To further assess long-term protective effects of iFTn-MR4 on cardiac IR injury, we divided IR mice into four groups for three doses of treatments every two days via tail vein injection: PBS, iFTn-M4, iFTn-R4 and iFTn-MR4 (Supplementary Fig. 6a). After 28 days post-surgery, the structure and function of hearts were evaluated by M-model ECHO imaging (Fig. 6c). Assessment of left ventricle functional parameters, including LVEF, LVFS, LVEDd and LVEDs, demonstrated a gradual improvement in the recovery of cardiac functionality after treatment with iFTn-M4, iFTn-R4 and iFTn-MR4 (Fig. 6d). Notably, various parameters of cardiac functions in the iFTn-MR4-treated group were comparable to that in the sham group. Subsequently, histological assessment of tissue fibrosis was performed using Masson's trichrome staining at 28 days after IR surgery (Fig. 6e). Compared to PBS, iFTn-M4 and iFTn-R4, iFTn-MR4 exhibited increased interstitial and perivascular fibrosis. Quantification analysis of the scar area relative to left ventricle area demonstrated that approximately 30% fibrosis relative to left ventricle was observed in mice treated with PBS, whereas iFTn-M4, iFTn-R4, and iFTn-MR4 were effective in reducing fibrosis to 14%, 16% and 9%, respectively. The protective effect of the nanozymes on cardiac hypertrophy was also evaluated by Wheat germ agglutinin (WGA) staining. Confocal imaging of cross-sectional area in IR tissue illustrated marked enlarged cardiomyocytes (green) compared to sham tissue (Fig. 6f). In comparison with the PBS group, all IR cardiac tissue treated with nanozymes displayed recovery of cardiomyocyte hypertrophy, with iFTn-MR4 showing the maximal recovery status. Additionally, H&E staining of major organs suggested that there was no apparent accumulation toxicities or damage in the evaluated organs (Supplementary Fig. 7). Long-termed toxicity assessments, conducted with a dosage and frequency four times greater than therapeutic assays over a period of one month, also revealed no significant signs of toxicity in the treated animals (Supplementary Fig. 8).

https://doi.org/10.1038/s41467-025-56414-8

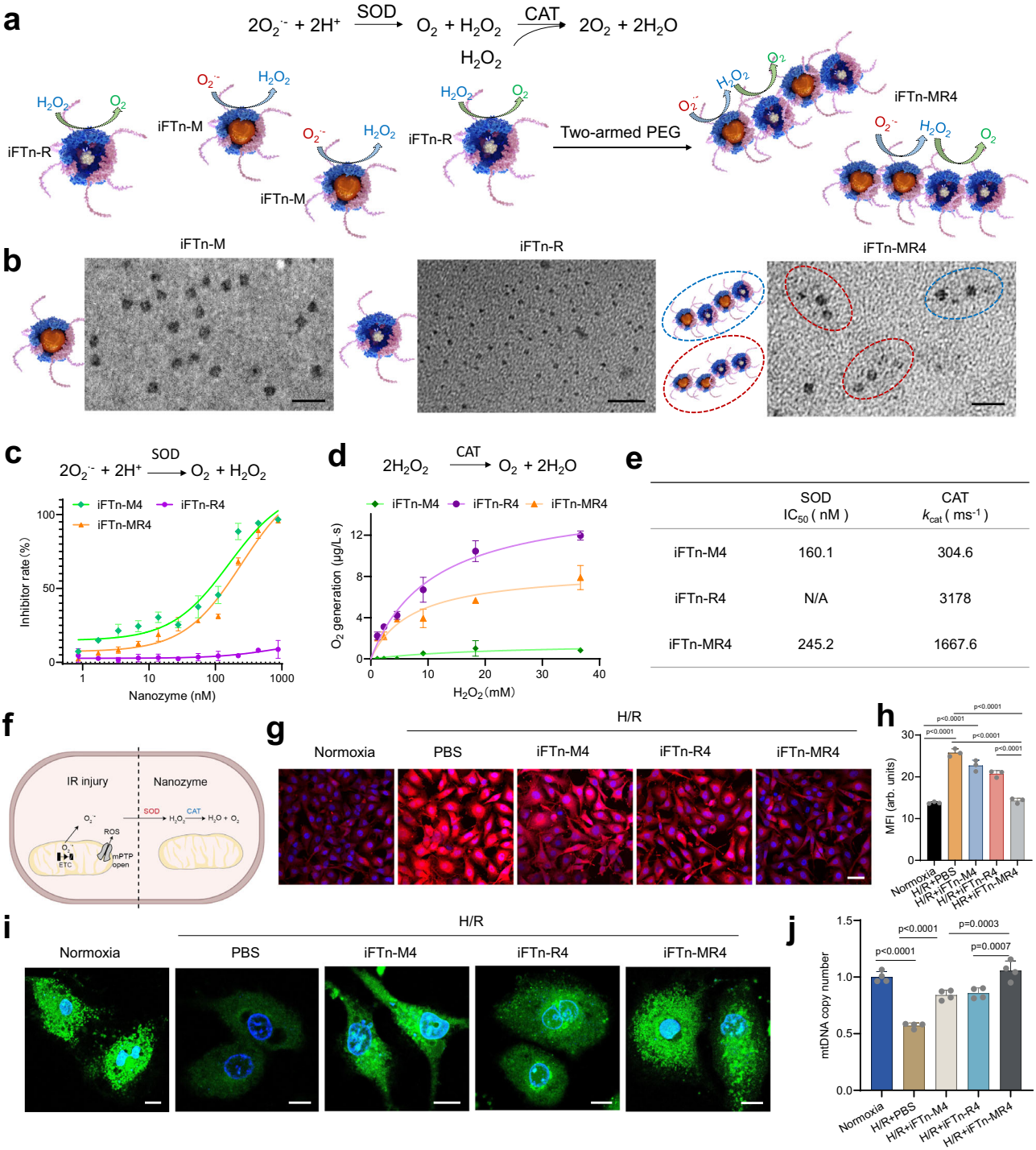

Fig. 5 | In vitro cascade reaction and mitochondrial protective function of iFTn-MR4. a Schematic illustration depicting the cascade catalytic reactions of iFTn-MR4 for the removal of $O_2^{\cdot-}$ and H_2O_2. iFTn-MR4 was constructed by assembling the same molar ratio of iFTn-M with SOD-mimicking activity and iFTn-R with CAT-mimicking activity through a two-armed PEG crosslinker. **b** TEM images of iFTn-M (left), iFTn-R (middle) and iFTn-MR4 (right). iFTn-MR4 was assembled from iFTn-M and iFTn-R of different sizes. Scale bar = 20 nm. **c** The relative SOD-like activity of iFTn-M4, iFTn-R4 and iFTn-MR4 under the same conditions ($n = 3$ independent experiments). **d** Kinetics for CAT-like activity of iFTn-M4, iFTn-R4 and iFTn-MR4 nanozyme under the same condition ($n = 3$ independent experiments). **e** The parameters of enzyme catalytic efficiency, IC_{50} values and k_{cat} were used to describe SOD- and CAT-like activities of various nanozymes, respectively. **f** Schematic illustration demonstrating the conversion of superoxide anion into nontoxic H_2O and O_2 by the constructed iFTn-MR4 nanozymes, capable of mimicking the cascade reaction of SOD and CAT. **g** Representative confocal images showing intracellular O_2 levels using $[Ru(dpp)_3]Cl_2$, and its luminescence is strongly quenched by molecular oxygen. Scale bar = 20 μm. **h** Quantification analysis of the luminescence of $[Ru(dpp)_3]Cl_2$ quenched by O_2 generated by indicated nanozymes ($n = 3$ biologically independent experiments). MFI refers to the Mean Fluorescence Intensity. **i** Representative confocal images of mPTP opening in H9C2 cells under normal conditions and H/R-induced oxidative stress following treatment with various treatments. Scale bar = 10 μm. **j** qPCR analysis of mtDNA copy number in H9C2 cells under normal condition and H/R-induced oxidative stress following different treatments ($n = 4$ biologically independent experiments). Data are presented as mean values ± SD. p values are calculated using one-way ANOVA with Tukey's multiple comparisons test without adjustments (**h**, **j**). Source data are provided as a Source Data file.

https://doi.org/10.1038/s41467-025-56414-8

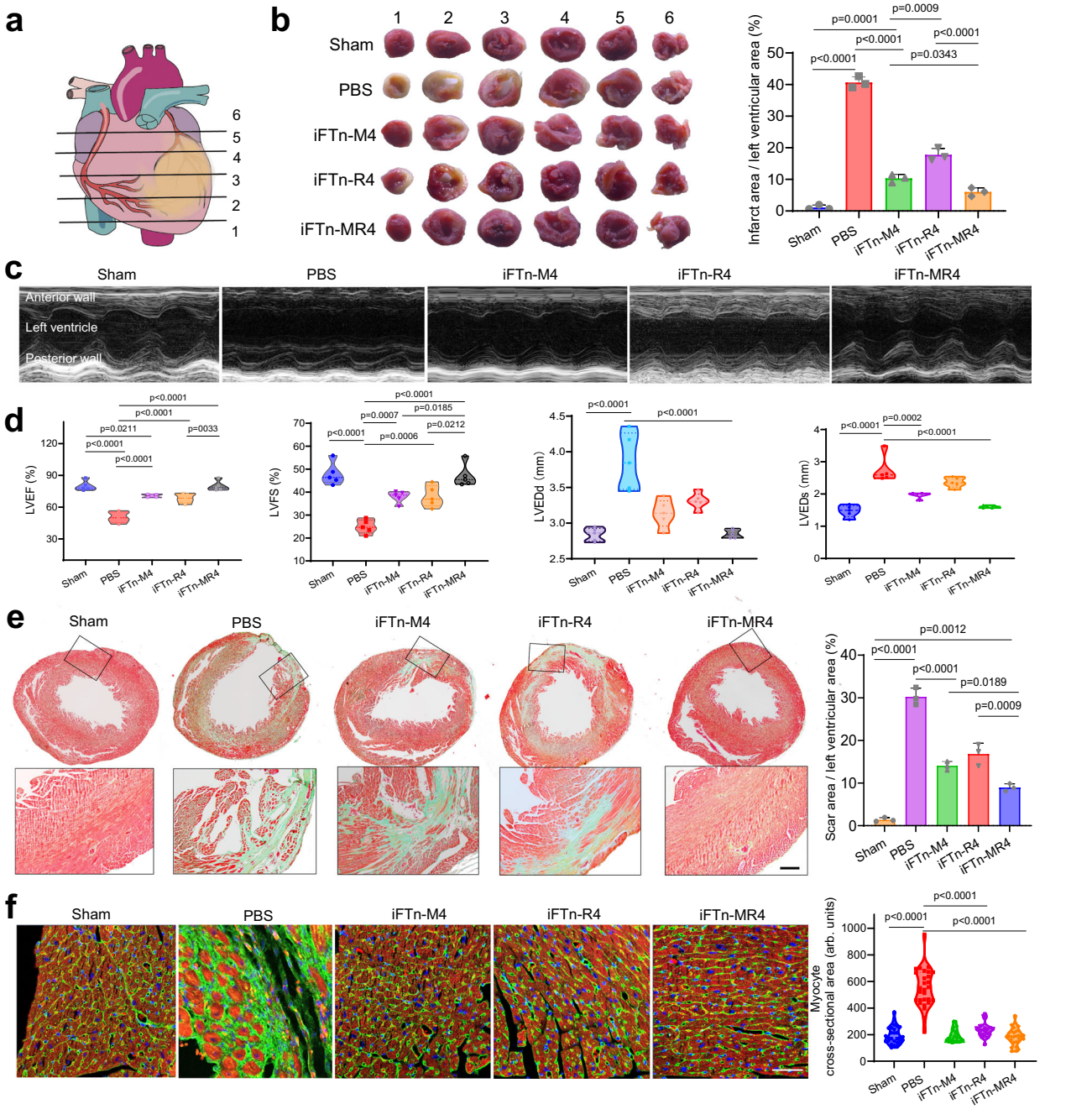

Fig. 6 | In vivo cardiac protection of iFT-MR4 in mouse IR model. a Schematic representation illustrating the cutting of 6 sections from the apex to the level of ligation. **b** Representative images (left) and image-based quantification analysis (right) of 6 cardiac sections without or with different treatments. The sections were stained using TTC for imaging the infarct area (white). The injury level was determined by calculating the percentage of the infarct area relative to the left ventricular area ($n = 3$ in each group). **c** Representative ECHO images of the left ventricular wall motion in mice with or without treatments 28 days after IR surgery. **d** Quantification analysis of cardiac functional recovery by determining the parameters of LVEF, LVFS, LVEDd and LVEDs ($n = 5$ mice for each group). **e** Representative images (left) and quantitative analysis (right) of midpapillary regions of the hearts, 28 days after IR using Masson's staining (green represents collagen-rich scar tissue; red represents viable myocardium). Right showing quantification analysis of the injury level by calculating the percentage of the scar area relative to the left ventricular area ($n = 3$ mice for each group). Scale bar = 100 μm. **f** Representative images (left) and image-based quantification analysis (right) of cardiomyocyte hypertrophy in cardiac injury regions by immunostaining with anti-α-Actin antibody (red) and Wheat germ agglutinin (WGA) staining (green) at 28 days after treatments ($n = 28$ technical samples examined over 3 mice per group). Scale bar = 100 μm. Data are presented as mean values ± SD. p values are calculated using one-way ANOVA with Tukey's multiple comparisons test without adjustments (**b**, **d**–**f**). Source data are provided as a Source Data file.

Mechanisms of iFTn cascade nanozymes for mitigating tissue damage

To gain deeper insights into the mechanisms underlying the protective effect of iFTn cascade nanozymes against IR injury, we conducted RNA sequencing (RNA-Seq) analysis to elucidate the gene expression profiles in mouse hearts subjected to myocardial IR injury. The gene expression analysis was performed at 3 days post-surgery following two doses of nanozyme treatments with PBS, iFTn-M4, iFTn-R4, or iFTn-MR4. Venn Diagrams demonstrated that 85% of differentially expressed genes in iFTn-M4 (*vs.* PBS) and 72% in iFTn-R4 (*vs.* PBS)

https://doi.org/10.1038/s41467-025-56414-8

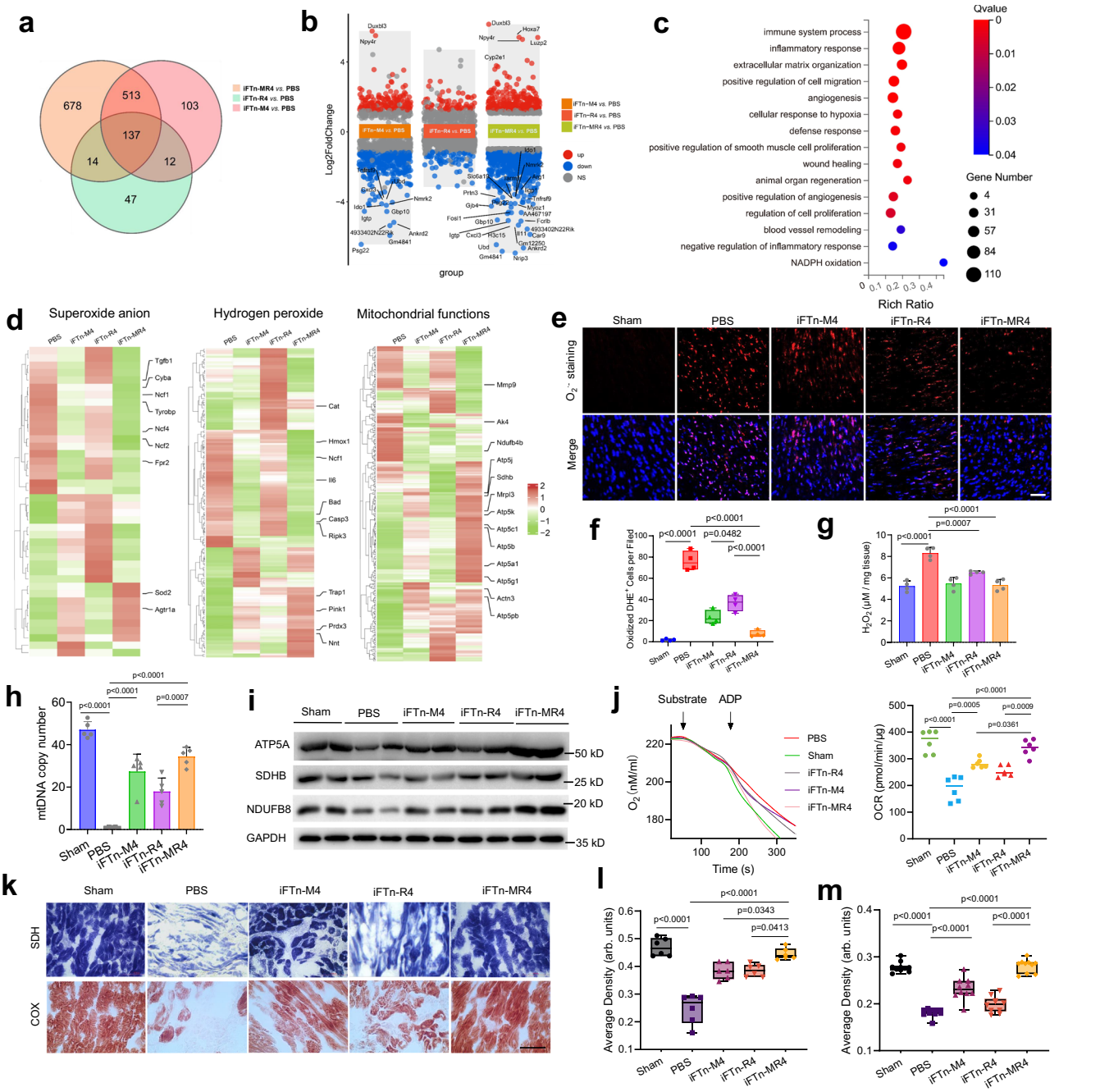

Fig. 7 | RNA-sequencing analysis of mechanisms of iFTn-MR4 for mitigating tissue damage. a Venn diagrams illustrating the relationship of differentially expressed genes (DGEs) between indicated groups. **b** Volcano plot displaying the results of the differential expression analysis. **c** Cluster profiler functional annotation showing GO enrichment analysis of DEGs, with the groups reflecting main categories of GO terms. **d** Heatmaps depicting the expression of genes related to superoxide anion, hydrogen peroxide, and mitochondrial functions in different groups. Confocal images (**e**) and quantitative analysis (**f**) of $O_2^{\cdot-}$ levels in the IR-damaged area from the sham or treated tissue ($n = 4$ mice per group). Scale bar = 50 μm. **g** Quantitative analysis of H_2O_2 in sham and IR tissues after various treatments ($n = 4$ mice per group). **h** qPCR analysis of mtDNA copy number in IR tissues after different treatments ($n = 5$ mice per group). **i** Western blot analysis of ATP5A, SDHB, and NDUFB8 in tissues with various treatments ($n = 2$ mice per group). **j** Analysis of mitochondrial respiration from isolated left ventricle tissue showed the oxygen consumption curve, smoothed using a spline fit with GraphPad Prism software (left). The OCR are presented on the right ($n = 6$ for each group). The images (**k**) and quantitative analysis of enzymatic activity assays of SDH (**l**) and COX (**m**) in both sham and IR model heart tissues following various treatments, $n = 6$ (**l**) or 10 (**m**) technical samples examined over 3 mice per group. Scale bar = 50 μm. Data are presented as mean values ± SD. The box plots showing the minima, maxima, centre, bounds of box and whiskers and percentile (**f**, **l**, **m**). p values are calculated using one-way ANOVA with Tukey's multiple comparisons test without adjustments (**f**–**h**, **j**, **l**, **m**). Source data are provided as a Source Data file.

overlapped with those in iFTn-MR4 (*vs.* PBS) (Fig. 7a), indicating that iFTn-MR4 induces changes in gene expression that combine patterns observed in iFTn-M4 and iFTn-R4. The distinct gene expression signatures among the iFTn-M4 (*vs.* PBS), iFTn-R4 (*vs.* PBS) and iFTn-MR4 (*vs.* PBS) are depicted in Fig. 7b, with significant up-regulated genes (red) and down-regulated genes (blue). Using these differentially expressed genes, a Gene Ontology (GO) enrichment analysis was conducted to assess the potential functional improvements conferred by iFTn-MR4. As shown in Fig. 7c, fifteen GO terms related to tissue repair are enriched in iFTn-MR4-treated hearts compared to PBS,

mainly including extracellular matrix organization, blood vessel regeneration and remodeling, inflammatory responses, and cellular response to hypoxia. We next analyzed the expression patterns by clustering all differentially expressed genes in the RNA-Seq data. The heatmap image illustrated the alteration of expressing patterns of these genes in PBS-, iFTn-M4-, iFTn-R4-, and iFTn-MR4-treated IR hearts (Supplementary Fig. 9). In comparison to the PBS group, iFTn-MR4 induced opposite gene expression patterns, implying functional recovery of IR hearts following iFTn-MR4 treatment. In contrast, iFTn-M4 or iFTn-R4 alone caused changes in only a subset of genes that were altered in iFTn-MR4-treated IR hearts. Further analysis revealed that these differentially expressed genes were associated with superoxide anion, hydrogen peroxide and mitochondrial functions (Fig. 7d). Importantly, iFTn-MR4 induced substantial changes in all listed three aspects of genes compared to PBS-treated IR hearts, whereas different levels of changes were observed in these genes with iFTn-M4 or iFTn-R4 alone. For examples, a significant increase/decrease in the expression of genes associated with superoxide anion, hydrogen peroxide and mitochondrial functions, such as *Ncf1*, *Trap1*, *Sdhb* and *Atp5a1*, was observed in both iFTn-M4 and iFTn-R4 groups compared to the PBS group. This trend was further enhanced in iFTn-MR4-treated hearts subjected to IR injury. These results implied the synergistic role of iFTn-MR4 in protecting IR hearts by combining therapeutic benefits of iFTn-M4 and iFTn-R4 in mediating superoxide anion, hydrogen peroxide and mitochondrial functions.

To further validate the protective mechanisms of the nanozymes, we assessed superoxide anion-, hydrogen peroxide- and mitochondria-associated functions in IR-injured tissue. Following different treatments in IR mice, we analyzed the levels of $O_2^{\cdot-}$ and H_2O_2 in sham and IR tissue, respectively. DHE histological analysis revealed that nanozyme treatments effectively decreased $O_2^{\cdot-}$ levels in IR tissue (Fig. 7e). Compared to the 80 oxidized DHE^+ cells per field in PBS-treated IR cardiac tissue, the oxidized DHE^+ cells of iFTn-M4, iFTn-R4 and iFTn-MR4 were decreased to 28 and 8, respectively (Fig. 7f). Quantification analysis of isolated IR cardiac tissue illustrated that, compared to other treatments, the iFTn-MR4 exhibited the lowest H_2O_2 levels, indicating that the cascade reaction effectively removed H_2O_2 from the IR tissue, as expected (Fig. 7g). The protective effect of iFTn nanozymes on mitochondrial functions was further analyzed. qPCR analysis of mtDNA copy number within sham and IR cardiac tissues demonstrated significantly elevated mitochondrial functional recovery following iFTn-MR4 treatment compared to PBS, iFTn-M4, and iFTn-R4 (Fig. 7h). Western blot analysis of mitochondrial oxidative phosphorylation complexes, including Complex II: ubiquinone oxidoreductase (SDHB), Complex I: NADH Ubiquinone Oxidoreductase Subunit B8 (NDUFB8), and Complex V: F1F0 ATP synthase (ATP5A) confirmed that the expression levels of ATP5A, SDHB, and NDUFB8 were substantially restored in IR tissue following nanozyme treatments, particularly with iFTn-MR4 (Fig. 7i). Moreover, mitochondria isolated from the left ventricle tissue of mice showed significantly higher state 3 oxygen consumption rates (OCR) in the iFTn-MR4-treated group compared to the PBS, iFTn-M4 and iFTn-R4 groups, indicating enhanced mitochondrial respiration function (Fig. 7j). Further histological analysis of SDH and COX enzyme activities revealed significant recovery of mitochondrial function in the IR injury tissue after iFTn-MR4 treatment (Fig. 7k-m).

Discussion

In this study, we constructed ionizable protein nanocages using a genetic engineering approach, enabling the assembly of a series of precisely controlled chain-like iFTn. These iFTn assemblies exhibited endosome-escaping capabilities, making them well-suited for customizing free radical-scavenging nanozymes for certain requirements in intracellular microenvironments, such as SOD and CAT activities to mitigate ROS damage. Our results support the advantages of iFTn nanozyme assemblies over monomeric nanozyme alone or non-ionizable counterparts in mitigating IR-induced cardiac tissue injury by taking advantage of their SOD-mimicking activity. Using the optimal tetrameric iFTn, we also biomimetically designed tetrameric cascade nanozymes (i.e., iFTn-MR4) with both SOD- and CAT-like activities. These ionizable cascade nanozymes provided several advantages: i) they overcame the intracellular endo-lysosomal barrier for efficient escape into the cytoplasm, crucial for harnessing SOD- and CAT-like activities while avoiding potential excess free radical production in endo-lysosomes; ii) they preferential accumulated in IR damaged tissue after systemic delivery, possibly attributed to enhanced vascular permeability and elevated FTn receptor expression in ischemic tissue; and iii) they maintained oxidative stress homeostasis and protected mitochondria against oxidative injury by converting produced free radicals ($O_2^{\cdot-}$ and H_2O_2) into nontoxic O_2 and H_2O. Additionally, unlike previously developed small molecular SOD/CAT cascade enzyme mimetics[32], iFTn nanozymes offer unique advantages inherent to nanomaterials, such as targeting delivery to disease sites and improved retention in IR-injured tissue. Together, these combined benefits empowered iFTn cascade nanozymes with the capability to effectively protect against oxidative injury in a mouse cardiac IR model following systemic delivery.

The endo-lysosomal barrier poses a significant hurdle for efficient intracellular delivery, typically resulting in less than 1% of payloads being released into the cytoplasm[33,34]. Effective endo-lysosomal escape is equally crucial for nanozyme delivery, as nanozymes generate free radicals in acidic conditions rather than scavenging them[35], irrespective of the type of enzyme-mimicking activity possessed by the nanozymes. Inspired by the development of ionizable lipids, a significant contribution of this study lies in the creation of ionizable nanozymes (i.e., iFTn) by genetically introducing repeated ionizable Histidine (pKa ~ 6.0) on the outer surface of protein nanocages. As the endosomes mature (pH 5.0–5.5), the ionizable property allows the nanozyme to transition from negative to protonated and positively charged, leading to localized disruption of the endosomal lipid bilayer and subsequent escape of the nanozyme into the cytoplasm. To enhance the in vivo performance of nanozymes and showcase the versatility of nanozyme design, we conducted a proof-of-concept study assembling diverse chain-like iFTn nanozymes using a two-armed PEG crosslinker. This assembly method effectively mediates the ionizable capability of the iFTn nanozymes, playing a crucial role in modulating their endosomal escape ability. Future studies could potentially improve the ionizable effect of the iFTn nanozymes by precisely manipulating the number and distribution of ionizable repeated Histidine on the outer surface of each FTn through genetic engineering approaches. In summary, the study presents an innovative approach to design nanozymes for combating oxidative tissue injuries and provides new insights into tailoring next generation of ionizable nanomedicines.

Methods

All animals work were handled in accordance with the policies and guidelines of the Animal Ethics Committee of Nankai University (2022-SYDWLL-000170). Mice were provided ad libitum access to food and water and housed in a specific pathogen-free (SPF) environment (a 14-hour light/10-hour dark cycle, temperatures of ~18-25 °C with 40-60% humidity).

Preparation and characterization of iFTn

For the preparation of FTn and iFTn in this study, three expression vectors were constructed through genetic engineering method. Firstly, the gene encoding the human ferritin heavy chain was cloned into the pET21a plasmid, resulting in the construction of a pET21a-FTn vector. Secondly, the nucleotide sequence of $9H_2E$ (i.e., $(HHE)_9$ peptide) was incorporated into the ferritin heavy chain gene using overlap extension PCR. The resulting recombinant gene was then inserted into the

pET21a, yielding the pET21a-9H_2E·FTn expression vector. Thirdly, both the ferritin heavy chain gene and 9H_2E-incorporated ferritin heavy chain gene was inserted into multiple cloning site 1 and multiple cloning site 2 of the pRSFDuet plasmid, creating the pRSFDuet-FTn-9H_2E·FTn vector. Subsequently, the resulting plasmids were transformed or co-transformed into *E. coli BL21(DE3)* to generate engineered bacteria for the expression of protein nanocages. The nanocages can be assembled in *E. coli* through the 24 expressed subunits, and thus various nanocages containing varying proportions of FTn/iFTn subunits were obtained by adjusting the combinations of the three constructed vectors. Specifically, the transformation of the pET21a-FTn vector led to the expression of 0% H_2E-FTn (0% ionizable heave chain subunits), while the pET21a-9H_2E·FTn vector expressed 100% H_2E-FTn (100% ionizable heave chain subunits). Transformation with the pRSFDuet-FTn-9H_2E·FTn resulted in the expression of 50% H_2E-FTn nanocages (50% ionizable heave chain subunits). Co-transformation of pET21a-FTn and pRSFDuet-FTn-9H_2E·FTn yielded 30% H_2E-FTn (30% ionizable heave chain subunits), and Co-transformation of pET21a-9H_2E·FTn and pRSFDuet-FTn-9H_2E·FTn produced 70% H_2E-FTn nanocages (70% ionizable heave chain subunits). Afterward, protein expression and purification were conducted in accordance with our previously published protocols[21,25]. Briefly, induction of protein expression was achieved by the addition of 1 mM isopropyl β-D-thiogalactoside (IPTG) at 20 °C for 8 hours. After removing undesired proteins through cell lysis and heating at 60 °C, the collected supernatant underwent further purification via gel-filtration chromatography using a Superose 6 column (Cytiva). The concentration of various nanocages was quantified using a bicinchoninic acid protein assay kit (PC0020-500, Solarbio). Molecular weights and sizes of various nanocages were determined by SDS–polyacrylamide gel electrophoresis (PAGE). Zeta potentials of various nanocages were measured using a Zetasizer Nano ZE (Malvern Instruments). For structural analysis of FTn protein, PyMOL v.2.3.2 based on PDB ID 3AJO was employed.

Nanozyme synthesis within iFTn

The nanozyme was synthesized through the in-situ growth of metal nano-particles/clusters within the hollow cavity of iFTn. To generate the iFTn-M or FTn-M nanozyme, the iFTn or FTn was dissolved in a 100 mM NaCl buffer, achieving a concentration of 0.2 mg/ml. $MnCl_2$ solution was then added dropwise (about 50 µl /min) using a peristaltic pump while maintaining a protein to Mn^{2+} molar ratio of 1:2000. The whole process was conducted under an argon atmosphere to prevent O_2 exposure. Simultaneously, H_2O_2 was introduced as an oxidizing agent in a 1:2 ratio (Mn^{2+}:H_2O_2), and 50 mM NaOH was added to neutralize emerging hydrogen ions. Upon completion of the reaction, 300 mM sodium citrate was added to chelate any residual metal ions. For the synthesis of iFTn-R nanozyme, 2 mg iFTn was diluted in a 150 mM NaCl solution until reaching a concentration of 0.2 mg/ml. Dissolve the $RuCl_3$ (40 µg) in water and was then added, and the mixture was stirred at room temperature for 1 hour. Unbound metal ions were subsequently removed using a PD-10 column (Cytiva). The resulting Ru-bound iFTn was reduced by the addition of $NaBH_4$. Finally, the obtained iFTn-M and iFTn-R nanozymes were further purified using a PD-10 column subjected to phosphate-buffered saline (PBS).

Assembly of iFTn or iFTn nanozymes

Assembly of iFTn or iFTn-nanozymes were accomplished using a PEG crosslinker (two-armed PEG-SCM, 10 KDa). Through the reaction of two-armed PEG-SCM with the free amines of the protein, iFTn was interconnected, and subsequent purification of different assemblies was conducted with Native-PAGE. Typically, the two-armed PEG-SCM was added into the iFTn solution (pH 8-9) at a molar ratio of 15:1 (PEG:iFTn), allowing the reaction to proceed overnight. The resulting assemblies were then isolated using Native-PAGE. Various iFTn assemblies with different molecular weights were carefully excised and pulverized in PBS buffer to facilitate the release of assemblies from the gels, respectively. The assembly of iFTn nanozymes followed the same procedure, with iFTn being replaced by iFTn nanozymes in the reaction. The morphology of various assemblies was characterized by TEM (HT7700, HITACHI) following negative staining with 1% uranyl acetate. Molecular weights and sizes of various assemblies were determined by Native–PAGE and size-exclusion chromatography (SEC). For SEC measurements, the PBS (0.1 M, pH 7.2) was used as the solvent.

Intracellular behaviors of iFTn

To assess cellular uptake, the 50% confluent H9C2 cells/primary mouse neonatal cardiomyocytes were initially incubated with 20 µg/ml Cy5-labeled iFTn and its assemblies for 2 hours. For confocal imaging studies, the cells were fixed with 4% paraformaldehyde for 15 minutes, followed by staining with phalloidin to label the cytoskeleton and subsequent DAPI staining for the nucleus. The cells were then observed using confocal microscopy (Zeiss, LSM710). To quantitatively assess cell uptake, flow cytometry analysis of the collected cells was conducted by measuring the signal intensity of Cy5 (BD, Calibur). The gating strategy for flow cytometry was shown in Supplementary Fig. 10a.

To investigate the ability of iFTn and its assemblies to escape from endo-lysosomes, about 50% confluent H9C2 cells were firstly incubated with Cy5-labeled iFTn and its assemblies (20 µg/ml) for 2 hours. Afterward, the medium was replaced with fresh culture medium, and the cells were incubated for an additional 2 hours. Subsequently, the cells were stained with 50 nM LysoTracker Red (Thermo Fisher Scientific) and Hoechst 33342 at 37 °C for 30 minutes. To compare the dynamic colocation of FTn-4er/iFTn-4er with lysosomes and their escape dynamics, H9C2 were allowed to uptake Cy5-labeled FTn-4er/iFTn-4er for 2 hours, followed by further culture for 0, 1, 2, 3, and 4 hours in fresh medium, with staining using LysoTracker Red and Hoechst 33342 at 37 °C for 30 minutes. The lysosomal localization of iFTn and its assemblies were examined using Zeiss LM710 confocal microscopy with excitation/emission wavelengths of 405/461 nm for nucleus, 565/578 nm for lysosome, and 633/670 nm for iFTn and its assemblies. The quantitative assessment of co-localization between iFTn/its assemblies with lysosomes was performed by determining Pearson's coefficients using the Just Another Colocalization Plugin (JACoP) within the ImageJ software (NIH).

Intracellular free radical detection

The assessment of ROS levels under hypoxia-reoxygenation (H/R) treatment to induce oxidative stress was conducted using the 2′,7′-Dichlorodihydrofluorescein diacetate (DCFH-DA) probes. Firstly, the 60% confluent cells were per-treated with various nanozymes at a concentration of 50 µg/ml for 4 hours. Subsequently, H9C2 cells/primary mouse neonatal cardiomyocytes were exposed to 1% O_2, 5% CO_2 and 95% N_2 in IR-mimicking solution (5 mM HEPES, 1 mM 2-DG, 139 mM NaCl, 12 mM KCl, 0.5 mM $MgCl_2$, 1.3 mM $CaCl_2$, and 20 mM Lactic acid, pH 6.2) for 6 hours to induce hypoxia, then reoxygenation (21% O_2 and 5% CO_2) with the addition of fresh DMEM with 10% FBS at 37 °C, for a total 6 h of reoxygenation. The control cells were kept under normoxia conditions. Following this, 50 µM DCFH-DA was added and allowed to incubate for 30 minutes at 37 °C. Confocal microscopy was then utilized to capture images of the cells. For the quantification analysis of ROS levels, flow cytometry was employed to record the signal of the DCFH-DA probes under the same conditions (Beckman, Cytoflex).

For the detection of intracellular $O_2^{\cdot-}$, Dihydroethidium (DHE) served as a peroxide indicator. Upon dehydrogenation by peroxides, DHE reacts with RNA or DNA for nucleus staining, producing red fluorescence. H9C2 cells exposed to H/R-induced oxidative stress were pretreated with 50 µg/ml nanozymes for 4 hours. Fluorescence images were observed under a confocal microscope with excitation/emission

wavelengths of 565/578 nm. Quantification analysis was also conducted by determining the signal intensity of the probes using flow cytometry (Beckman, Cytoflex). The gating strategy for flow cytometry was shown in Supplementary Fig. 10b.

Evaluation of enzyme-mimicking activity

The SOD-mimicking activity of iFTn-nanozymes was assessed followed the manufacturer's instructions (Dojindo). The absorbance of the resulting product, water-soluble tetrazolium salt-1 (WST-1) formazan, was measured at 450 nm using a Multiskan FC microplate spectrophotometer (Thermo Fisher Scientific). SOD-like activity and kinetic curves were derived from the inhibition percentage of the WST-1 reaction with $O_2^{\cdot-}$.

To evaluate the CAT-mimicking activity of different iFTn-nanozymes, oxygen generation from enzymatic reactions was monitored using a dissolved oxygen meter. Initially, H_2O_2, acting as the substrate for CAT, was dissolved in a phosphate buffer (pH 7.8) over a concentration range of 0-37 mM. Oxygen levels in the solution were recorded at 5-second intervals with the dissolved oxygen meter. Once stable readings were obtained, the nanozymes were introduced at a final concentration of 0.2 mg/ml. Oxygen measurements continued for 5 minutes following the onset of the enzymatic reaction. Subsequently, kinetic curves were plotted based on reaction rates at varying substrate concentrations to determine CAT-like activity.

Electron paramagnetic resonance

To examine the ability of iFTn-M4 to scavenge $O_2^{\cdot-}$, xanthine/xanthine system was used to generate $O_2^{\cdot-}$ in PBS buffer (10 mM, pH 7.4) [7]. The xanthine/xanthine system were prepared with 1 mM xanthine, 0.05 U/ml xanthine oxidase (XOD), and 1 mM diethylenetriaminepentaacetic acid (DTPA). After adding 0.5 μM iFTn-M4 or PBS to the system, the reaction was started by the addition of XOD. 100 mM BMPO was used to trap $O_2^{\cdot-}$ by forming the BMPO/·OOH adduct. The EPR measurements were carried out using a Bruker EMXnano spectrometer (Billerica, MA) at ambient temperature.

Detection of mitochondrial permeability transition pore

Mitochondrial permeability pore (mPTP) opening was assessed using the fluorescent probe calcein AM. In a typical procedure, H9C2 cells were seeded on a cover slip with a 50% confluent and exposed to H/R-induced oxidative stress. After three washes with PBS, the cells were treated with 50 μg/ml various iFTn nanozymes for 4 hours. Following staining with 10 μM calcein AM for 30 min, a 20 μM $CoCl_2$ water solution were added to quench the fluorescence of calcein AM outside the mitochondrial, which is a result of the limited diffusion of Co^{2+} from cytosol to mitochondria when the mPTP is in the "off" state. Following fixation with 4% PFA, the nuclei were stained with DAPI. Subsequently, confocal microscopy was employed to capture images of cells subjected to different treatments.

Long-term toxicity study

The female C57BL/6 mice, aged 6-8 weeks, were obtained from SPF (Beijing) biotechnology Co. Ltd. All animal procedures were conducted in accordance with the guidelines for the care and use of laboratory animals approved by Animal Ethics Committee of Nankai University. Mice were randomly divided into 5 groups ($n = 4$ per group): PBS control, iFTn, iFTn-M4, iFTn-R4 and iFTn-MR4. The control group received the PBS only, while the treatment groups received iFTn and iFTn-based nanozymes at doses of 10 mg/kg body weight via intravenous (*i.v.*) injection every two days for 24 days. Mice were observed daily for any signs of toxicity. Body weights were recorded at baseline and then every 2 days throughout the study period. After 30 days of the treatment, mice were anesthetized with isoflurane and blood was collected via cardiac puncture for hematological analyses. Mice were then euthanized by cervical dislocation, and major organs (liver, kidneys, spleen, heart, lungs) were harvested, and fixed in 4% paraformaldehyde for histopathological examination. Hematological parameters were measured using an automated hematology analyzer. Fixed tissues were processed, embedded in paraffin, sectioned at 5 μm thickness, and stained with hematoxylin and eosin (H&E) for microscopic evaluation.

Ischemia-reperfusion (IR) mouse model

C57BL/6 (female, 8 weeks) mice were purchased from the Laboratory Animal Center of the Academy of Military Medical Sciences (Beijing, China). The mice IR model was established through ligation of the left anterior descending coronary artery, following the procedure outlined in our previous report[18]. In brief, mice were anesthetized with 1.5% isoflurane in combination with O_2 and subsequently mechanically ventilated using an anesthetic machine (MicroVent 1, Hallowell EMC). After a left thoracotomy at the fourth intercostal space, the left coronary artery (LAD) was ligated for 30 minutes, followed by reperfusion achieved by removing the 7 - 0 silk suture. The sham mice underwent a similar surgery, excluding the LAD ligation.

In vivo biodistribution of various iFTn

The in vivo biodistribution and accumulation of various iFTn in the IR heart was assessed using an in vivo imaging system. Briefly, mice subjected to IR or sham surgery were intravenously administered with Cy5-labeled iFTn-Ner at the onset of reperfusion. At post-administration intervals of 12 and 24 hours, the heart and other major organs were harvested and subjected to ex vivo imaging using an IVIS Spectrum imaging system (IVIS Lumina II Xenogen, Caliper Life Sciences). The levels of various iFTn accumulation in different organs were quantified by measuring the mean signal intensity within the region of interest (ROI). At the 24-hour time point, the hearts were harvested, frozen, and subsequently cryosectioned to a thickness of 15 μm. Selected sections were immunostained with a phycoerythrin (PE)-labeled anti-CD31 antibody (BioLegend). Tissue accumulation imaging was conducted using a confocal laser scanning microscope (LSM710, Zeiss), with excitation/emission wavelengths of 405/461 nm for nucleus, 565/578 nm for blood vessels, and 633/670 nm for iFTn or its assemblies. Following the acquisition of all images, the cardiac panorama was reconstructed using Adobe Photoshop 2023 software.

Mitochondrial DNA (mtDNA) copy number

The mtDNA copy number assay was employed to evaluate the protective effect of various iFTn nanozymes on mitochondrial function in the presence of oxidative stress. H9C2 cells were exposed to hypoxia-reoxygenation (H/R)-induced oxidative stress. After three times washes with PBS, the cells were incubated with iFTn nanozymes for 4 hours. Following incubation, the cells were collected, and their total DNA was extracted using the Universal DNA Extraction Kit (Tiangen Biotech). For heart tissues, the IR and sham hearts were harvested after two-doses of treatment with nanozyme or PBS. The tissues were then homogenized, and total DNA was extracted using the Universal DNA Extraction Kit. Real-time PCR was utilized to assess the mtDNA copy number. The cycle threshold (Ct) values of a mitochondrial-specific target (MT-CO2) and a nuclear-specific target (ACTB) were determined. The relative mtDNA copy number was calculated as the ratio of MT-CO2 to ACTB.

The primers sequences for mtDNA copy number were as follows. MT-CO2: Forward 5′-CCTCCCATTCATTATCGCCGCCCTTGC-3′; Reverse 5′-GTCTGGGTCTCCTAGTAGGTCTGGGAA-3′. ACTB: Forward 5′-ATCC GTAAAGACCTCTATGCCAACA-3′ ; Reverse 5′-GGCTACAACTACAGGGC TGACCAC-3′.

In vivo free radical detection

To evaluate the in vivo superoxide-scavenging capability of nanozymes, DHE was utilized as a superoxide probe for histological

examination. Following two doses of treatment, heart tissues were cryosectioned and incubated with DHE (5 μM) for 30 minutes at 37 °C. Subsequently, after staining with DAPI, images were acquired using a confocal microscope (LSM 710, Zeiss). The DHE-positive cells were quantified using ImageJ software. For H_2O_2 detection, heart tissues were collected and homogenized on the third day post-treatments. The concentration of H_2O_2 per gram of tissue was then determined using a commercial kit (Beyotime Biotechnology) following the manufacturer's instructions.

Therapeutic evaluation

To assess the therapeutic potential of various iFTn-M nanozymes, mice with IR and sham models were randomly assigned to five groups: sham, FTn-M4, iFTn-M1, iFTn-M2, and iFTn-M4. Treatments were administered through *i.v.* tail vein injections with an equivalent protein concentration of 2.5 mg/kg. A total of three doses were given (on days 0, 2, and 4). At 1 day, 3 days, and 28 days post-IR or sham surgery, cardiac functions were assessed using an echocardiographic system equipped with a Vevo2100 echocardiographic system (VisualSonics). Cardiac tissue fibrosis and collagen-rich scar formation were assessed through Masson's trichrome staining following the standard protocol, and images were captured using a light microscope. Quantitative analysis of the healthy tissue area was conducted using ImageJ.

For the evaluation of acute heart IR, the infarct size was assessed by triphenyltetrazolium chloride (TTC) staining. The mouse models were divided into five groups: Sham, IR treated with PBS, iFTn-M4, iFTn-R4, and iFTn-MR4. Treatment involves two doses administrated via tail vein injection at day 0 and day 2, each containing 2.5 mg/kg of iFTn nanozymes (equivalent protein concentration). After a 3-day treatment, the hearts were sectioned into six transverse slices and these slices were incubated in 1% TTC in sodium phosphate buffer at 37 °C for 20 min. The infarct region was identified by white area, and the infarct size was determined by analyzing images using ImageJ.

For the therapeutic evaluation of iFTn-M4, iFTn-R4, and iFTn-MR4, IR and sham mouse models were administered in three doses via tail vein injection, each containing 2.5 mg/kg of iFTn nanozymes. Following the assessment of cardiac functional with echocardiographic system (VisualSonics), the isolated cardiac IR tissue subjected to different treatments underwent further investigation. Mitochondrial function was evaluated through western blotting, using mitochondrial oxidative phosphorylation (OXPHOS) (Abcam, ab110413) as the target and glyceraldehyde-3-phosphate dehydrogenase (GAPDH) as the internal control protein. The analysis of mtDNA copy number, superoxide free radicals and H_2O_2 in cardiac IR tissue was conducted following the aforementioned protocols. For the quantitative analysis of cardiomyocyte size, sections were stained with FITC-wheat germ agglutinin (WGA) and anti-Actin antibody to delineate the cell membrane and cytoskeleton, respectively. The images were observed and recorded using confocal microscopy, and the cardiomyocyte size was analyzed using ImageJ. Systemic toxicities were assessed through hematoxylin and eosin (H&E) staining following standard procedures.

Mitochondrial isolation and measurement of OCR

To evaluate mitochondrial function during the early stages of iFTn-nanozyme treatment, IR model mice were administrated two doses of PBS, iFTn-M4, iFTn-R4, or iFTn-MR4 via *i.v.* tail vein injections on days 0 and 2 (protein concentration, 2.5 mg/kg). On the third day post-IR and treatment, mitochondria were isolated from the left ventricle of sham and IR model hearts using a mitochondrial isolation kit (C3606, Beyotime). Mitochondrial protein concentration was measured using a Bradford Protein Quantification Kit (P0009, Yeasen). Oxygen consumption measurements were performed in the Oxytherm$^+$ Liquid-phase oxygen electrode system (Hansatech) according to the previous method with slight modification[36]. Briefly, freshly isolated mitochondria were added to the Oxytherm$^+$ electrode chamber containing 1 ml respiration buffer (120 mM KCl, 5 mM KH_2PO_4, 3 mM HEPES, 1 mM EGTA, and 0.3% defatted BSA, pH 7.2). To initiate the reaction, 10 μl succinate (10 mM, pH 7.2) and 10 μl rotenone (100 μM) were added using microsyringes. Mitochondria oxygen consumption rate (OCR) was measured following the sequential injections of 10 μl adenosine diphosphate (ADP, 10 mM).

Histological assessment of SDH and COX activity

The heart tissues were collected and immediately embed the tissue in OCT compound, and section it at 10 μm thickness. The sections were incubated in the SDH staining solution (5 mM EDTA, 1.5 mM NBT, 100 mM sodium succinate, and 0.2 mM PMS in PBS, pH=7.0) at 37 °C for 30 minutes. After 4 times wash with PBS, the slides were dehydrated with graded ethanol and clearing with xylene. In term of COX staining, the reaction mixture containing 100 μM cytochrome c, 0.1% DAB, and 2 μg/ml bovine catalase in 0.1 M phosphate buffer (pH 7.4). The slides were incubated with reaction buffer for 40 minutes at 37 °C, followed by washing 4 times and mounting with glycerol-gelatin aqueous slide mounting medium (Solarbio). The images were captured using a Leica DM3000 microscope, and quantitative analysis was conducted using ImageJ software (NIH). The average density of SDH and COX staining was calculated as the integrated optical density relative to the area within the tissue sections.

RNA-sequencing analysis

To understand the mechanisms underlying the protective effect of nanozymes against IR injury, RNA-sequencing analysis was conducted. Mouse IR models were established following treatment with PBS, iFTn-M4, iFTn-R4 and iFTn-MR4 for two doses (equivalent protein concentration of 2.5 mg/kg) given every other day. After three days, RNA was extracted from the isolated cardiac IR tissue subjected to various treatments. Sequencing was performed on the DNBSEQ platform. The raw RNA-seq reads were aligned to the mouse genome (GRCm38) by HISAT2 (v2.1.0). After alignment, the number of reads for each gene model was obtained and normalized as Transcripts Per Kilobase Million mapped fragments (TPM). Subsequently, differentially expressed genes (DEGs) between iFTn-M4 *vs.* PBS, iFTn-R4 *vs.* PBS, and iFTn-MR4 *vs.* PBS were identified with $|\log2\ FC\ (\text{fold change})| \geq 1.2$, coupled with an adjusted false discovery rate ≤ 0.05. Venn diagram, volcano plot and heatmaps were generated using R (Bioconductor, Roswell Park Cancer Institute, Buffalo NY, USA).

Statistics and Reproducibility

All data graphs and analysis were generated using GraphPad Prism 9, and group differences were evaluated using one or two-way ANOVA with Tukey's multiple comparisons test without adjustments. The statistical parameters and the number of sample size subjects used per experiment are found in the figure legends. Each experiment was performed for at least 3 times to make sure similar results are reproducible.

Reporting summary

Further information on research design is available in the Nature Portfolio Reporting Summary linked to this article.

Data availability

The RNA-sequencing data generated in this study have been deposited in the Gene Expression Omnibus database under accession code GSE282015. The full image dataset is available from the corresponding author upon request. The source data generated in this study are provided in the Supplementary Information/Source Data file. Source data are provided with this paper.

References

1. Hausenloy, D. J. & Yellon, D. M. Ischaemic conditioning and reperfusion injury. *Nat. Rev. Cardiol.* **13**, 193–209 (2016).
2. Chouchani, E. T. et al. Ischaemic accumulation of succinate controls reperfusion injury through mitochondrial ROS. *Nature* **515**, 431–435 (2014).
3. Cadenas, S. Mitochondrial uncoupling, ROS generation and cardioprotection. *Biochim Biophys. Acta Bioenerg.* **1859**, 940–950 (2018).
4. Kuznetsov, A. V. et al. The role of mitochondria in the mechanisms of cardiac ischemia-reperfusion injury. *Antioxid. (Basel)* **8**, 454 (2019).
5. Granger, D. N. & Kvietys, P. R. Reperfusion injury and reactive oxygen species: The evolution of a concept. *Redox Biol.* **6**, 524–551 (2015).
6. de la Fuente, M. et al. Enzyme therapy: current challenges and future perspectives. *Int. J. Mol. Sci.* **22**, 9181 (2021).
7. Wu, J. et al. Screening of protein-based ultrasmall nanozymes for building cell-mimicking catalytic vesicles. *Small* **18**, e2202145 (2022).
8. Wang, C., Liu, Q., Huang, X. & Zhuang, J. Ferritin nanocages: a versatile platform for nanozyme design. *J. Mater. Chem. B* **11**, 4153–4170 (2023).
9. Huang, Y., Ren, J. & Qu, X. Nanozymes: classification, catalytic mechanisms, activity regulation, and applications. *Chem. Rev.* **119**, 4357–4412 (2019).
10. Gao, L. et al. Intrinsic peroxidase-like activity of ferromagnetic nanoparticles. *Nat. Nanotechnol.* **2**, 577–583 (2007).
11. Lin, Y., Ren, J. & Qu, X. Catalytically active nanomaterials: a promising candidate for artificial enzymes. *Acc. Chem. Res* **47**, 1097–1105 (2014).
12. Zhuang, J. et al. Machine-learning-assisted nanozyme design: lessons from materials and engineered enzymes. *Adv. Mater.* **36**, e2210848 (2024).
13. Fan, K. et al. In vivo guiding nitrogen-doped carbon nanozyme for tumor catalytic therapy. *Nat. Commun.* **9**, 1440 (2018).
14. Wang, Z. et al. Biomimetic nanoflowers by self-assembly of nanozymes to induce intracellular oxidative damage against hypoxic tumors. *Nat. Commun.* **9**, 3334 (2018).
15. Li, S. et al. A nanozyme with photo-enhanced dual enzyme-like activities for deep pancreatic cancer therapy. *Angew. Chem. Int Ed. Engl.* **58**, 12624–12631 (2019).
16. Xi, J. et al. Copper/carbon hybrid nanozyme: tuning catalytic activity by the copper state for antibacterial therapy. *Nano Lett.* **19**, 7645–7654 (2019).
17. Huang, Y. et al. Self-assembly of multi-nanozymes to mimic an intracellular antioxidant defense system. *Angew. Chem. Int Ed. Engl.* **55**, 6646–6650 (2016).
18. Zhang, Y. et al. Biomimetic design of mitochondria-targeted hybrid nanozymes as superoxide scavengers. *Adv. Mater.* **33**, e2006570 (2021).
19. Wei, H. & Wang, E. Nanomaterials with enzyme-like characteristics (nanozymes): next-generation artificial enzymes. *Chem. Soc. Rev.* **42**, 6060–6093 (2013).
20. Wu, J. et al. Nanomaterials with enzyme-like characteristics (nanozymes): next-generation artificial enzymes (II). *Chem. Soc. Rev.* **48**, 1004–1076 (2019).
21. Huang, X. et al. Protein nanocages that penetrate airway mucus and tumor tissue. *Proc. Natl Acad. Sci. USA* **114**, E6595–E6602 (2017).
22. Lin, X. et al. Hybrid ferritin nanoparticles as activatable probes for tumor imaging. *Angew. Chem. Int Ed. Engl.* **50**, 1569–1572 (2011).
23. Zhen, Z. et al. Ferritin nanocages to encapsulate and deliver photosensitizers for efficient photodynamic therapy against cancer. *ACS Nano* **7**, 6988–6996 (2013).
24. Liang, M. et al. H-ferritin-nanocaged doxorubicin nanoparticles specifically target and kill tumors with a single-dose injection. *Proc. Natl Acad. Sci. USA* **111**, 14900–14905 (2014).
25. Zhu, M. et al. Machine-learning-assisted single-vessel analysis of nanoparticle permeability in tumour vasculatures. *Nat. Nanotechnol.* **18**, 657–666 (2023).
26. Liu, Q. et al. Modular assembly of tumor-penetrating and oligomeric nanozyme based on intrinsically self-assembling protein nanocages. *Adv. Mater.* **33**, e2103128 (2021).
27. Kalyanaraman, B. et al. Measuring reactive oxygen and nitrogen species with fluorescent probes: challenges and limitations. *Free Radic. Biol. Med.* **52**, 1–6 (2012).
28. Zhang, X. et al. Biomimetic design of artificial hybrid nanocells for boosted vascular regeneration in ischemic tissues. *Adv. Mater.* **34**, e2110352 (2022).
29. Chouchani, E. T. et al. A unifying mechanism for mitochondrial superoxide production during ischemia-reperfusion injury. *Cell Metab.* **23**, 254–263 (2016).
30. Diez-Silva, E., Kato, M., Dao, G. J. & Suresh, M. S. Kinetics of sickle cell biorheology and implications for painful vasoocclusive crisis. *Proc. Natl Acad. Sci. USA* **112**, 1422–1427 (2015).
31. Stansfield, W.E. et al. Chapter 4 - The pathophysiology of cardiac hypertrophy and heart failure. In: *Cellular and Molecular Pathobiology of Cardiovascular Disease* (eds Willis MS, Homeister JW, Stone JR). Academic Press (2014).
32. Doctrow, S.R. et al. Salen manganese complexes mitigate radiation injury in normal tissues through modulation of tissue environment, including through redox mechanisms. In: *Redox-Active Therapeutics* (eds Batinić-Haberle I, Rebouças JS, Spasojević I). Springer International Publishing (2016).
33. Liu, S. et al. Membrane-destabilizing ionizable phospholipids for organ-selective mRNA delivery and CRISPR-Cas gene editing. *Nat. Mater.* **20**, 701–710 (2021).
34. Zhao, Y. et al. Nanomechanical action opens endo-lysosomal compartments. *Nat. Commun.* **14**, 6645 (2023).
35. Liang, Q. et al. A metal-free nanozyme-activated prodrug strategy for targeted tumor catalytic therapy. *Nano Today* **35**, 100935 (2020).
36. Cristina, S. G. et al. An optimized protocol for coupling oxygen consumption rates with β-oxidation in isolated mitochondria from mouse soleus. *STAR Protoc.* **2**, 100735 (2021).

Acknowledgements

This work was supported by the National Natural Science Foundation of China, including 82072054 (J.Z.), 32271448 (X.H.), 32425032 (X.H.), 82472134 (J.Z.), 82402481 (X.Z.). X.H. was also funded by the National Key Research and Development Program of China (2022YFA1105100) and Tianjin Synthetic Biotechnology Innovation Capacity Improvement Project (TSBICIP-KJGG-014-03).

Author contributions

Q.L., J.Z., and X.H. conceived the idea, collected data and conducted data analysis. Q.L., Z.G., and X.Z. performed all experiments. Q.D., Y.Z., and M.Z. assisted to conduct animal studies. R.L. and L.J. help acquire confocal images. D.K. and A.C.M helped supervise experiments and revised the manuscript. D.K., J.Z., and X.H. designed and supervised all studies. Q.L., J.Z., and X.H. wrote the manuscript.

Competing interests

The authors declare no competing interests.

Additional information

Supplementary information The online version contains supplementary material available at https://doi.org/10.1038/s41467-025-56414-8.

Correspondence and requests for materials should be addressed to Deling Kong, Jie Zhuang or Xinglu Huang.

Peer review information : *Nature Communications* thanks Yeong-Renn Chen, and the other, anonymous, reviewer(s) for their contribution to the peer review of this work. A peer review file is available.